Matilde de Jesus Jacob Alves

Licenciada em Ciências da Engenharia Física

Assembly of a portable X-ray fluorescence spectrometer with tri-axial geometry

Dissertação para obtenção do Grau de
Mestre em Engenharia Física

Orientador: Doutora Sofia Pessanha,
Prof[a]. Auxiliar Convidada,
Universidade NOVA de Lisboa

Co-orientador: Doutor Mauro Guerra, Prof. Auxiliar Convidado,
Universidade NOVA de Lisboa

Júri:

Presidente: Doutora Maria Isabel Simões Catarino, Universidade NOVA de Lisboa

Arguentes: Doutora Alda Sofia Pessanha de Sousa Moreno, Universidade NOVA de Lisboa
Doutor Pedro Manuel Ferreira Amorim, Universidade de Lisboa

FACULDADE DE
CIÊNCIAS E TECNOLOGIA
UNIVERSIDADE NOVA DE LISBOA

Abril, 2016

Assembly of a portable X-ray fluorescence spectrometer with tri-axial geometry

All science is either physics or stamp collecting.
Ernest Rutherford

Acknowledgements

I would like to extend my gratitude to both of my supervisors, Professor Sofia Pessanha and Professor Mauro Guerra for their effort and support in materializing this project, and for all the learning opportunities they provided me with.
I would like to express my very great appreciation to Professor Maria Luísa Carvalho for her expertise and advice that were so valuable in this project, and for the motivation she always provided.
I would like to offer my special thanks to Dr. João Veloso from the I3N research center of the physics department of the University of Aveiro, for lending us the power supply for the X-ray tube, it was crucial for all the data acquisition present in this thesis.
Furthermore, I would like to express my acknowledgements to Mario Costa, for allowing us to analyze the paper document from his private collection, and that was a fundamental part of this thesis case-studies.
Moreover, the assistance provided by all the colleagues and professors of the lab was also greatly appreciated. I wish to acknowledge the help provided by the Physics Department Workshop for all their work and skills that contributed to the design of this spectrometer.

On a more personal level, I would like to thank my family: my mother, Maria Filomena Jacob, and my grandparents, Argemira and António Jacob, for all their love and support throughout all my life and for their encouragement in making me strive for success, I owe it all to you; my boyfriend, Micah Kassner, for his love, patience, and motivation, and for always making me smile.

I would also like to thank all of my friends who have always been there for me, particularly in this more stressful times: João Pires and Margarida Nascimento, for all the breaks you made me take from the thesis, Isabel Allegro, for her amazing friendship and for always cheering me up and João Lourenço, for all the coffee breaks and the irreplaceable help he gave in many technical aspects of this dissertation.

Abstract

X-ray fluorescence (XRF) technique is a powerful analytical tool with a broad range of applications such as quality control, research of environmental contamination by heavy metals, studies regarding cultural heritage, among others.
In this dissertation, a portable energy dispersive X-ray fluorescence (Energy Dispersive X-Ray Fluorescence (EDXRF)) spectrometer will be developed, with orthogonal tri-axial geometry between the X-ray tube, the secondary target, and the sample. Said geometry reduces the background of the obtained spectrum by removing the *Bremsstrahlung* from the tube through polarization effects. Moreover, a practically monochromatic excitation energy is obtained. This geometry renders a better peak-background ratio, thus improving the detection limits, leading to superior sensitivity.The use of this geometry has proven to be more advantageous when dealing with the detection of trace elements in low-Z matrix samples. Moreover, the use of a portable setup is of paramount importance in studies related with Cultural Heritage and archaeometry. Thereafter, two case studies will be presented concerning the analysis of a 18th century paper document and the bone remains of an individual buried in the early 19th century.

Keywords: X-Ray Fluorescence, Tri-axial Geometry, Portability, *In Situ*.

Resumo

A técnica de fluorescência de Raios-X é uma ferramenta analítica poderosa com uma vasta gama de aplicações, tais como controlo de qualidade, pesquisa de contaminação do meio ambiente por elementos pesados, estudos sobre o património cultural, entre outros. Nesta dissertação será desenvolvido um espectrómetro portátil de fluorescência de raios-X dispersivo em energia, com geometria ortogonal tri-axial entre o tubo de raios-X, o alvo secundário, e a amostra. Esta geometria reduz o fundo do espectro obtido através da remoção do *Bremsstrahlung* por efeitos de polarização. Ademais, é obtido um feixe de energia praticamente monocromático. Esta geometria garante uma melhor razão pico-fundo, melhorando deste modo os limites de deteção, o que conduz a uma sensibilidade superior. A utilização desta geometria provou ser mais vantajosa na deteção de elementos traço em amostras constituída por matrizes de baixo número atómico, Z. Além do mais, o uso de uma configuração portátil é de suma importância em estudos relacionados com o património cultural e arqueometria. Consequentemente, dois estudos de caso serão apresentados: a análise de um documento em papel do século 18, e a análise de restos mortais ósseos de um indivíduo enterrado no início do século 19.

Palavras-chave: Fluorescência de Raios-X, Geometria Tri-axial, Portabilidade, *In Situ*.

Contents

List of Figures

List of Tables

List of Acronyms

ADC Analogue-to-Digital Converter.

COPRA Compact Röntgen Analyser.

DAQ Data Acquisition.

DL Detection Limits.

DPP Digital Pulse Processor.

EDXRF Energy Dispersive X-Ray Fluorescence.

EPD Electronic Personal Dosimeters.

FDA U.S. Food and Drug Administration.

FWHM Full Width at Half Maximum Height.

ICP-AES Inductively Coupled Plasma Atomic Emission.

NCRP National Council on Radiation Protection and Measurements.

NID Negligible Individual Dose.

NIST National Institute of Standards and Technology.

PIXE Particle Induced X-ray Emission.

ROI Region of Interest.

SDD Silicon Drift Detector.

XRF X-Ray Fluorescence.

1 Introduction

1.1 Motivation

This thesis purpose is to build a portable X-Ray Fluorescence (XRF) spectrometer with tri-axial geometry in between the X-ray tube, the secondary target and the sample. The XRF technique is a powerful analytical tool with a broad spectrum of applications such as quality control, research of environmental contamination by heavy elements, studies of cultural heritage, and others. Portable XRF spectrometers, in particular, possess an extensive range of applications resulting predominantly from their portability, multi-element capability, fast analysis times, minimal sample preparation requirements, and non-destructive nature [1]. Although the sensitivity of such spectrometers does not come as close as the sensitivity in non-portable laboratory instruments, the implementation of a tri-axial geometry promises an advantageous innovation when compared to other spectrometers of the same sort. Such technology offers a cheap and fast mean of analysis, moreover, it removes the need for sample transportation and storage [1] required in both forensic science and material research in cultural heritage analysis. Concerning the last field of applications, this spectrometer is of the utmost importance for authentication of an assortment of materials, like documents and other pigments materials, and also matching unidentified samples with reference materials (for example, to determine a sample authenticity or historical period) [2].

1.2 State-Of-The-Art

The X-ray Fluorescence (XRF) spectrometer resulting of this project, arises from the need to bridge portability and sensitivity with copious applications. The growing need to investigate forensic sciences samples and cultural heritage elements with non-destructive *in situ* techniques is the motivation that prompts this project. Miniaturization and removal of spatial constraints are significant limitations of this field of research due to the inability of moving the objects or to the impracticality of destroying the proof in forensic investigations [3]. XRF is a well settled laboratory technique and constitutes one of the few atomic

spectrometric techniques that can be used for portable instrumentation. As formerly described, there is a need to find a compromise between bench top spectrometer's high sensitivity and portability regarding XRF spectrometers. In academia and chemical analysis market, there is no shortage of portable spectrometers, but there is not yet one merging portability and tri-axial geometry results. Actually, compared to other portable atomic spectrometry techniques, portable XRF has better features like multi-element capability, a less destructive nature, greater simplicity, and more robustness [1]. Considering only portability, the options are numerous, for this is an area that has been evolving through the last decades. There are devices that allow *in situ* sampling and analysis of contaminated soil, like the Spectrace TN 9000 portable P-XRF, and have a better performance when compared to Inductively Coupled Plasma Atomic Emission (ICP-AES). Hence, it remains a useful and fit-for-purpose, powerful tool that provides precise and quick analytic results [4]. Other instruments like compact-XRF Compact Röntgen Analyser (COPRA), allow nondestructive and local analysis of microscopic samples with high elemental sensitivity that can be both used as a bench top unit in a laboratory and a transportable device for *in situ* measurements [2]. Also developed in lab was an Silicon Drift Detector (SDD) based XRF spectrometer, whose small size of the detection, excitation module, the elimination of the liquid nitrogen cryostat, and its resolution, makes this device ideal for portable high-resolution XRF spectrometers [5]. Other mobile XRF instrument developed, even though not usually accepted as portable, was focused on the optimization of the glancing angle for a portable total reflection XRF spectrometer. It was concluded that such field portable XRF could provide accurate data and consistent with reference method [6]. Bearing in mind only the tri-axial geometry aspect of XRF spectrometers, the options are more limited. Such experimental Energy Dispersive X-ray Fluorescence (EDXRF) spectrometers offer advantages such as simplicity of the associated instrumentation and high efficiency detection system. In this bench top laboratory devices, the X-ray tube, the secondary target and the sample are placed in a tri-axial geometry. Nevertheless, the instrumental design's simplicity, based in one X-ray tube, a solid state detector and a high voltage generator, does not imply elevated economic costs in the implementation in the industrial process [7]. After studying the role of X-ray reflectivity, coherent, and incoherent scattering in light samples, it was established that the tri-axial geometry is the best geometry for EDXRF apparatus to achieve the best peak-to-background ratio [8, 9]. Comparing two x-ray XRF spectrometers, a portable one and a non-portable one using a metallic Cu alloy as a reference, it was concluded that the detection limits are the main problem of the low-power portable spectrometers, but with more powerful x-ray tubes, the detection limits can be improved [10]. Another evaluation between portable and a stationary XRF spectrometers was performed, regarding scattering radiation for different matrices. It showed similar behavior for both spectrometers, but the portable system presented higher background [10]. Also, the choice of the detectors affects the device's performance: in a study of detection systems in portable XRF, the Amptek SDD was compared with other two devices, supplanting both. Showing that the fine tuning of the detector parameters

could improve the overall results for all detectors, and therefore, the general results [11]. Other factors can also improve the instrument's resolution. For instance, using a capillary X-ray lens with a new generation of low power micro-focus X-ray tube and a drift chamber detector enabled a portable unit for micro-XRF with a few tens of μm lateral resolution in a non-commercial-EDXRF [12]. In another example, an EDXRF was used to analyze different kinds of paper. This technique proved be a good elemental method to differentiate and classify samples [13]. In conclusion, this XRF spectrometer, allied with the engineered tri-axial strategy for ideal portability, all together with a compact design, and high sensitivity makes this instrument a viable alternative to other spectrometers in the market. Furthermore, its success is supported by previously made research, and other spectrometers that were already built and tested.

1.3 Goals and Work strategies

The ultimate goal of this dissertation is to design and build a portable EDXRF spectrometer with a tri-axial geometry, combining the advantages of portability with high sensitivity. To achieve this purpose, the work pursues the following steps:

- Careful planning and design of setup including the choice of materials for the secondary target, collimators, shielding and support pieces.
- Assembling of all the components, testing the existing instrumentation (such as the X-ray tube and detector), and testing different configurations until obtaining the most satisfactory results.
- Spectra acquisition of two groups of standard reference materials, and of two case studies: a paper document and human bone remains.
- Data analysis: detection limits, accuracy and elemental concentration calculations.

The work developed in this thesis was presented at the symposium - Heavy Metals: from the environment to the man, Costa da Caparica, Portugal, 2015, and at a conference poster session - Colloquim Spectroscopicum Internationale XXXIX, Figueira da Foz, Portugal, 2016.

2 Theoretical Background

2.1 X-ray

This chapter will cover the essential theoretical background of X-ray spectrometry physics. This topic is pertinent to grant an understanding of the core of this dissertation's basic concepts and focus especially on X-ray emission and production phenomena, as well as in other interaction processes. The X-ray is an electromagnetic radiation that can suffer refraction, reflection, diffraction, and polarization, is not affected by electrical and magnetic fields, and interacts with biological tissues. X-rays' wavelengths range from 0.01 to 10 nm, consisting in energies ranging approximately from 100 eV to 100 keV. From 5 to 10 keV, the region is named hard X-rays, and the lower energy range is named soft X-rays [14]. Wilhelm Conrad Röntgen is credited as being the discoverer of X-rays in Germany in 1895, and he was the first to systematically study them. Röntgen verified that crystals of barium platinocyanide turned luminescent when there was a discharge from a discharge tube in the vicinity. This occurred with the tube enclosed by black paper, demonstrating that his radiation could penetrate matter. Later, in 1913, Henry Moseley demonstrated that the wavelengths of the spectrum's lines were characteristic of the element of which the target was made, which led to scientists like Hevesy, Coster, and others, to investigate the potential of fluorescent X-ray spectroscopy as a form of qualitative and quantitative elemental analysis [14]. Currently, X-ray based methods, like X-ray fluorescence spectroscopy, are fundamental in industrial and medical fields and one of the most powerful and flexible techniques available for the analysis and characterization of materials [15]. In the case of this dissertation, XRF will be used in the qualitative and quantitative analysis of constituents of cultural heritage documents and archaeological artifacts.

2.1.1 X-ray Emission

X-rays' emission occurs when incident high energy particles, like photons, ions, or electrons, hit a target. Such phenomena can take place as two distinct atomic processes, the

emission of continuous radiation (*Bremsstrahlung*), and the emission of characteristic radiation.
Characteristic X-rays are emitted from heavy elements when their electrons perform transitions between the lower atomic energy levels. If the colliding particle has sufficient energy to remove an orbital electron from the inner electron shell of an atom, the electron from higher energy levels shall occupy the gap, therefore emitting X-ray photons, as seen in figure 2.1.

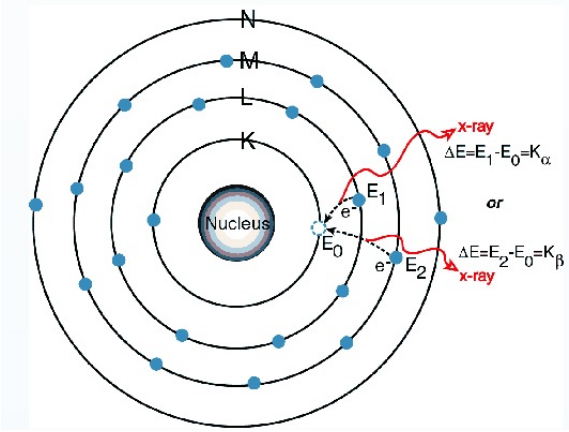

Figure 2.1: Schematic representation of XRF characteristic emission [16]

Such a process originates an X-ray emission spectrum constituted of spectral lines. These lines of discrete frequencies are also referred to as characteristic lines, for they hinge upon the element used as target. Each of these electronic transitions causes the emission of a photon X. The energy of this X photon is equal to the difference between the binding energy of the final levels E_f, and first E_i:

$$E_X = \mid E_f - E_i \mid \tag{2.1}$$

When high-energy-charged particles lose energy transiting through the Coulomb field of a nucleus, it emits a continuous spectrum of X-ray radiation, also known as *Bremsstrahlung* (from the German, meaning "deceleration radiation"). Electromagnetism theory dictates that the emission of radiation from the acceleration of charged particles, hence the deceleration of high energy charged particle penetrating a target must produce radiation. This continuous spectrum is characterized by a short-wavelength limit λ, that corresponds to the maximum energy of the excited electrons [14].

$$\lambda_{min} = \frac{hc}{eV_0} \tag{2.2}$$

Where h is Planck's constant, c is the velocity of light, e is the electron charge, and V_0 is the applied potential difference.

The *Bremsstrahlung* intensity distribuition is given by:

$$N(E)dE = kiZ\Big(\frac{E_{max}}{E} - 1\Big)dE \tag{2.3}$$

Where i is the tube current, Z is the atomic number of the target material, N(E)dE is the number of photons with energies between E and E+dE and k is a constant. This formula, demonstrates that the number of photons is inversely related to the energy E of the photons.

Occasionally, the energy might be first transferred to another electron in an higher shell, and then ejecting it from the atom in order to adjust to a more stable configuration, like in figure 2.2. This spontaneous process is called the Auger effect [17]. The energy of the ejected electron is given by:

$$E_e = \mid (E_f - E_i) \mid -E' \tag{2.4}$$

Being E_f the energy of the final state and E_i the energy of the initial state, and E' the bonding energy of the level from which the second electron was pulled.

The Auger's decay competes with the emission of a characteristic X-ray photon and occurs mainly in elements of lower atomic number (Z < 40) [18]. The probability of the Auger effect increases with a decrease in the difference of the corresponding energy states, and it is the highest for low Z elements [14]. If the vacancy is filled by an electron from a higher sub-shell from the same shell, the transition is entitled Coster-Krönig. A consequence of the Auger effect is that the number of X-ray photons produced from an atom is less than expected. The probability of a vacancy in an atomic shell or sub shell giving rise to a radiative transition is called fluorescence yield (ω), or the ratio of the number of X-ray photons emitted to the number of ionized atoms. The fluorescence yield is very low for low Z elements, hence why X-ray spectrometers are less sensitive for lighter elements [19].

2.1.2 X-ray Interaction with Matter

The interaction of radiation with matter depends on the atoms that constitute the material and the energy of the photons. The main processes involving the interaction of radiation with matter, like the photoelectric effect, X-ray scattering and pair production (the latest not being relevant for X-ray for it does not occur for E < 1 MeV [19]), shall be more thoroughly described in the following subsection.

2.1.2.1 X-ray Attenuation

The photoelectric effect and the Rayleigh and Compton interaction lead to the attenuation of the X-ray radiation. If an X-ray beam of intensity I_0 interacts with a layer of material

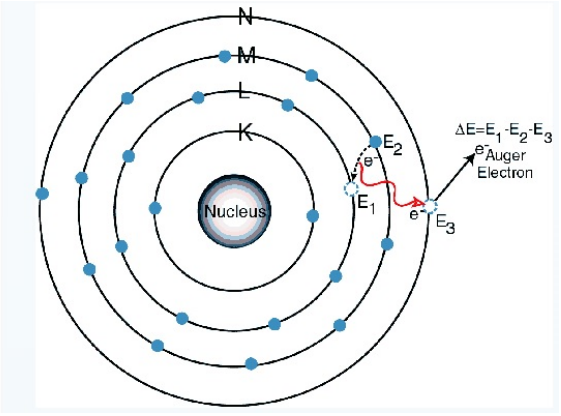

Figure 2.2: Schematic representation of Auger effect [16]

of thickness x, the attenuation of the intensity of the beam is described according to the Lambert-Beer law (figure 2.3):

$$I_x = I_0 e^{[-(\frac{\mu}{\rho}\rho x]} \tag{2.5}$$

where $\mu(cm^{-1})$ is the linear attenuation coefficient and $\frac{\mu}{\rho}$ (cm^2/g) is the mass-attenuation coefficient for material of density $\rho(g/cm^3)$. The intensity exponentially depends on the thickness of the layer. The mass attenuation coefficient $(\frac{\mu}{\rho})$ is a quantity that depends on the composition of the material and the energy of the X-ray photons.

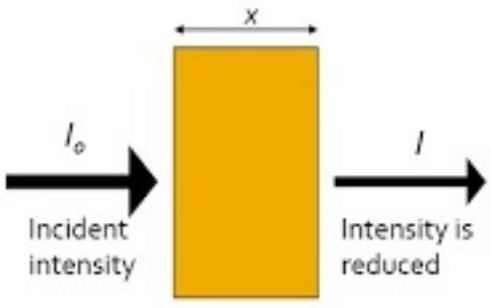

Figure 2.3: Lambert-Beer law Schematic representation for X-ray attenuation [20]

For low energies (below 1 MeV) the photoelectric effect is the central interactions of X-rays with matter. This phenomena occurs when a photon with energy equal or greater than the binding energy of the electron interacts with it. The incident photon is absorbed and an electron (photo-electron) is ejected with an energy equal to the difference between the original photon energy and the binding energy [14]:

$$E_X = \mid E_f - E_i \mid \tag{2.6}$$

The probability of the occurrence of such effect is maximum for photon energies in the order of the binding electron energy [18], and it depends on Z^4 for low energy photons and Z^5 to high energy photons [14].

Abrupt discontinuities in the photoelectric mass absorption coefficient (absorption edges) occur where the energy of the photons become higher than the binding energy of a particular shell [14]

The scattering of X-rays is triggered through two distinct processes: Rayleigh and Compton scattering. The Rayleigh scattering (coherent scattering) - a process by which photons are scattered by strongly bound atomic electrons and in which the atom remains in its ground state. Rayleigh scattering takes place typically at the low energies and for high-Z materials, it's probability being proportional to Z^2 [14, 21].
The Compton scattering (incoherent scattering) is the interaction of a photon with a loosely bound outer electron, that translates into a decrease in energy and a change of direction of the incoming photon, thus leading the electron to be ejected in a different direction, as shown in figure 2.4. The conservation of momentum and energy at the collision cause the photon's loss of energy.

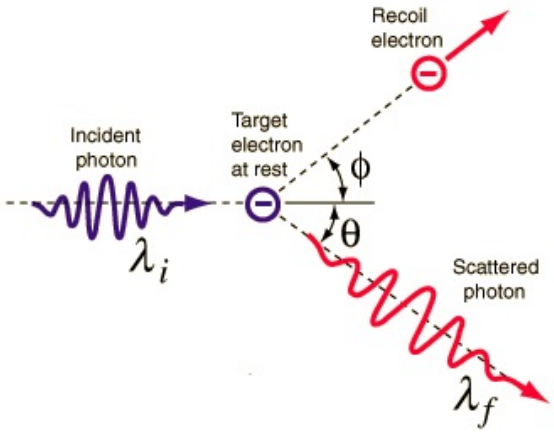

Figure 2.4: Schematic representation of the Compton scattering [22]

The Compton scattering can be described with equation 2.7, in which photon with the energy, E, bounces into another direction with energy, E', when deflected by an angle, Θ, while the electron keeps the remaining part of the energy $\Delta E = E - E'$:

$$\frac{E'}{E} = \frac{1}{1 + (1 - cos\Theta)} \frac{E}{E_e} \tag{2.7}$$

Being E_e the rest energy of an electron (511 keV).

The geometric setup of the sample, detector and X-ray tube is commonly arranged at 90°, for this is the angle that minimizes the elastic and inelastic scattering into the detector [8]. Regardless of the geometrical effects, the main responsible for diffusion in the matrix of the sample, and the total amount of Compton and Rayleigh scattering.

When added to the photoelectric mass absorption $(\tau\ \rho)$, these effects lead to the total mass attenuation coefficient (equation 2.2):

$$\frac{\mu}{\rho} = \frac{\tau}{\rho} + \frac{\sigma_{sct}}{\rho} \tag{2.8}$$

Where ($\frac{\sigma_{sct}}{\rho}$) is the mass-scatter coefficient (that takes into account both scattering effects). The mass attenuation coefficient (μ/ρ) is proportional to the total photon interactions cross-section per atom according to equation 2.9 [23]:

$$\frac{\mu}{\rho} = \frac{\sigma}{N_A} \tag{2.9}$$

Where A is the atomic weight ($gmol^{-1}$), N_A the Avogadro number (6.022×10^{23} atom mol^{-1}), and σ is the sum of the cross-sections for all the elementary scattering and absorption processes (barns/atom = 10^{-24} cm^2/atom).

Both Compton and Rayleigh scattering processes do not allow the identification of elements by the emission of characteristic radiation after the photoelectric effect. Nonetheless, these processes are accountable for increasing the background in the detector.

2.1.2.2 X-ray Reflection

When radiation crosses media with different refractive indexes it will be deflected from its original track (see figure 2.5), and the relation between the refractive indexes of the medium and the glancing angle is given by Snell's law:

$$n_1 sin\theta_1 = n_2 sin\theta_2 \tag{2.10}$$

Where n_1, n_2 are the refractive indexes of each medium.

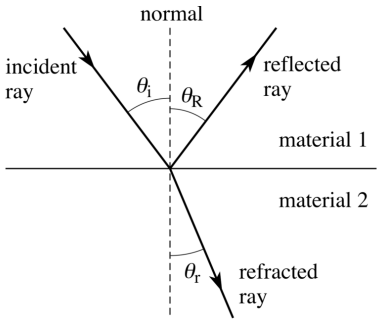

Figure 2.5: Schematic representation of incident, reflected and refracted beams at the interface of two media [24].

The refractive index can be written as a complex quantity:

$$n = 1 - \delta - i\beta \tag{2.11}$$

where the imaginary, β, is a measure of the attenuation, and $1 - \delta$, is the real part of the refractive index.The δ varies with the X-ray energy according to:

$$\delta = \frac{N_a}{2\pi} r_e \rho \frac{Z}{A} \lambda^2 \tag{2.12}$$

being the imaginary component:

$$\beta = \frac{\lambda}{4} \frac{\mu}{\rho} \rho \tag{2.13}$$

where (μ/ρ) is the mass attenuation coefficient. In the X-rays region, the value of δ is usually in the order of 10^{-6}, meaning that radiation is weakly refracted by any medium.

When the refraction angle, θ_r, is 90^o, the refracted beam will emerge tangentially to the surface's border. Thus, the correspondent angle of incidence is then named critical angle, θ_{crit} :

$$cos\theta_{crit} = \frac{n_2}{n_1} \tag{2.14}$$

When the angle with the interface is inferior to the critical angle, θ_{crit}, the incident beam is totally reflected in the first medium. Since θ_{crit} is very small its cosine can be approximated by:

$$\theta_{crit} \approx 1 - \frac{\theta_{crit} 4^2}{2} \tag{2.15}$$

If we take into account equation 2.14 and 2.12 and 2.15 :

$$cos\theta_{crit} = \frac{1,65}{E}\sqrt{\frac{Z}{A}\rho} \tag{2.16}$$

For low-medium atomic number elements,$A \approx 2Z$ so we have:

$$cos\theta_{crit} = \frac{1,17}{E}\sqrt{\rho} \tag{2.17}$$

Where E is the energy (keV), θ_{crit} is the critical angle in degrees, and ρ the density, in $g.cm^{-3}$.
The reflectivity of a material is given by the intensity ratio of the reflected and incident beam, and it is depending on energy of the beam. The reflectivity can reach 100 % around the critical angle, and it is inferior to 0.1 % for glancing angles of 1^o and more degrees.

2.1.3 X-ray Production and Detection

There are several techniques using X-rays aiming to identify the different elements present in a sample. The technique used in this dissertation, X-ray fluorescence, is only one of the many existing techniques that stand out, such as Electron Beam and Particle Induced X-ray Emission (PIXE).

In this dissertation, it was used an X-ray tube to produce X-rays, and its functioning will be described in the upcoming section.

2.1.3.1 X-ray Tube

A high-voltage X-ray tube has considerable benefits regarding safety and convenience. The vital parameters to take into account in a X-ray tube are the maximum high voltage and current, and the anode material (it is important that the anode is a good heat conductor).

Its basic instrumentation usually entails a radiation-shielding, an independent tungsten filament with a current control unit, a high-melting-point metallic anode, a high-voltage connection to the anode, a beryllium foil exit window, and a means of dissipating the produced heat [14]. In order to power the X-ray tube, a controllable, stable high-voltage power supply capable of providing typically between 5 to 60 kV and a low-voltage power supply for providing current to heat the filament are used.

The X-ray tube windows are typically made of beryllium (Be) due to their high transmission for low energy X-rays, although, Be windows tend to be very thin (foil thickness in the range of 50 to 250 μm [14]), which can lead to fracture [15]. According to the position of the anode and the Be window, we can differentiate reflection and transmission target with side-window (shown in figure 2.6) or end-window X-ray tubes respectively. In the scope of this work, we used a side-window geometry, which is suitable for both high-kV and high-power operation.
Regarding the output of the tube, the maximum intensity of the spectra $I'(\lambda)_{max}$ corresponds to the wave-length λ:

$$I'(\lambda)_{max} = I'(\lambda_{I_{max}}) \tag{2.18}$$

Being:

$$\lambda_{I_{max}} = \frac{3}{2}\lambda_{min} \tag{2.19}$$

Bearing in mind the energy-wavelength relation:

$$E = \frac{hc}{\lambda} \tag{2.20}$$

The relation can be written as:

$$E_{I_{min}} = \frac{2}{3}E_{max} \tag{2.21}$$

The total intensity of the spectra I' increases with the atomic number (Z) of the anode and the square applied voltage [18]:

$$I' = kZV^2 \tag{2.22}$$

k being a constant including the electrons electric current in the tube.

The critical value of voltage corresponds to the situation where the kinetic energy of the electrons is greater than the incident electron binding energy. In this case, there are well defined intense peaks overlapping the continuous spectrum, which constitute the radiation feature element of the anode [25].

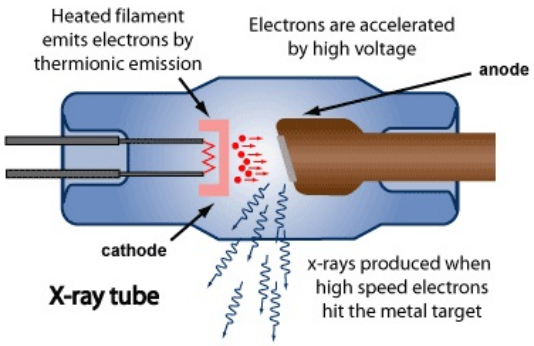

Figure 2.6: Schematic representation of a side-window X-ray tube [16]

2.1.3.2 Secondary Target and Tri-axial geometry

There are several mechanisms that minimize the background radiation, and it can be done by monocromatizing the maximum excitation radiation. This can be achieved with the use of a filter on the output of the X-ray tube with the appropriate atomic element in order to attenuate the low energy radiation. Another method to monocromatize the radiation is through the use of a secondary target which is excited by the beam of primary X-rays from the X-ray tube and whose characteristic radiation excites the sample. Both of these methods will not entirely monocromatize K_α radiation because the anode line, the K_β radiation, and high energy *Bremsstrahlung* continue to be transmitted, nonetheless, attenuated.
Another benefit connected with this method is the flexibility of choosing the excitation energy and allowing the detection of elements with low atomic number [14]. The combination of the anode and the secondary target should take into account the compromise between the energy of the X-rays emitted from the anode and the energy necessary to ionize electrons' shells of the secondary target [18].
Nevertheless, even with these mechanisms, part of the *Bremsstrahlung* is scattered into the detector, which increases the background and decreases the sensitivity of the spectrometer. Hence the need to resort to a tri-axial system.

X-ray radiation can be polarized by scattering [26]. For an unpolarized primary beam, scattering at an angle of $\pi/2$ results in a nearly complete plane polarization of the scattered X-rays [14, 21]. Through the use of collimators to define the three orthogonal beams, it was shown that signal-to-background ratios were enhanced. When X-ray radiation with energy in the range typically used in XRF, focuses on the secondary target, the *Bremsstrahlung* can be eradicated by scattering the beam at an angle of exactly $\pi/2$ [27]. Scattering this radiation from the secondary target by the sample to the detector will annihilate the remaining radiation. This way, barely any *Bremsstrahlung* radiation from the tube interacts with the detector, refining the signal-to-noise ratio [18]. Nonetheless, to achieve such angles, the beams must be exceedingly collimated, thus a compromise has to be made between the collimator apertures and the intensity of the resulting spectra.

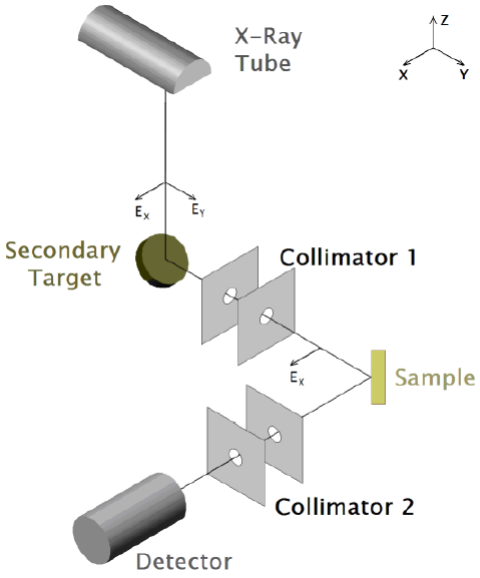

Figure 2.7: Schematic representation of the tri-axial geometry of the XRF spectrometer [28]

2.1.3.3 Collimation

A collimator is a device used to either attain a beam with limited cross section or to produce a beam of parallel rays [29]. In XRF setups, typically the X-rays exit the tube with a conical angular distribution of 100º - 150º. In order to reduce the cross section of the beam and re-position it, some sort of collimation is necessary [23].
Even though it has the disadvantage of reducing the beam's intensity, using collimators in a XRF setup narrows the beam to a central active region of the detector, hence diminishing effects such as incomplete charge collection and escape peaks. The collimator's material should absorb radiation in the range employed energies and should have an easily identifiable X-ray spectrum.

In the previous section, it was mentioned that the use of a collimator is of the utmost importance to guarantee the improvement of the signal-to-background radiation, for it enables only the selection of the radiation scattered at a 90º angle (relative to the primary beam). The enhancement of the signal-to-background ratio leads to an increased sensitivity, which allows us to identify trace elements present in the samples that are being analyzed [30, 31].

2.1.3.4 Detectors

The detectors mainly used in energy dispersive X-ray fluorescence are solid-state, high efficiency detectors that support simultaneous multi-elemental analysis, such as Si-PIN and Si-drift detectors SDD, that can be obtained from manufacturers like Vortex® [32], Amptek® [16], Ketek® [33], among others.
A good EDXRF detector must fulfill certain requirements such as a wide energy range and

linearity between the incoming photons and the output rate, and proportionality between the pulse and the incoming photon's energy. Other very important parameters to take into account are the energy resolution, the detection efficiency, and the sensitivity of the detector.
The sensitivity relies on several factors: the intrinsic noise (regulates the quantity of usable signal), the detector window (absorbs some of the incident radiation), and the detector cross-section and volume (calculate the probability of conversion of incident radiation into energy)[23].
The energy resolution measures the ability of the detector to discriminate between photons with very similar energy. This parameter can be indicated as the Full Width at Half Maximum Height (FWHM) of the measured distribution. A greater FWHM indicates a more challenging identification of peaks from photons with similar energies. [34].
The detection efficiency is given by the number of emitted photons that are completely absorbed by the detector [35].

2.2 Spectra

2.2.1 Notation

The characteristic lines in X-ray emission spectra correspond to atomic electronic transitions originated from the excitation of the sample. In order to understand the different spectral lines characteristic to the elements, one can use a set of rules: the Siegbahn notation [36]. According to this notation, X-ray spectra are classified as K, L, M... (and so on) series, corresponding, respectively, to the atomic levels of the radiative transitions K, L, M, of the emitted photons (see table 2.1). Each series has (2n - 1) transition levels. The K level constitutes the simpler spectra, for it does not decompose in various transition levels. Each one of the series has groups of lines, the more intense group being named α. As the intensity decreases, the groups are named β, γ, δ, etc. Due to the fact that the K and L series are the most intense, these are the best series for elemental characterization and identification, the K being more appropriate for lighter elements, and L for heavier elements and characterizing elements of the sample series [18].

Table 2.1: Some of the common electronic levels with Siegbahn and IUPAC notation [36].

High energy level	Low energy level	Name of the line	IUPAC notation
$K(1s^1)$	$L_3(2p^1_{3/2})$	$K\alpha_1$	$K - L_3$
	$L_2(2p^1_{1/2})$	$K\alpha_2$	$K - L_2$
	$M_3(3p^1_{3/2})$	$K\beta_1$	$K - M_3$
	$M_2(3p^1_{1/2})$	$K\beta_3$	$K - M_2$
$L_3(2p^1_{3/2})$	$M_5(3d^1_{5/2})$	$L\alpha_1$	$L_3 - M_5$
$L_2(2p^1_{1/2})$	$M_4(3d^1_{3/2})$	$L\beta_1$	$L_2 - M_4$
$M_5(3d^1_{5/2})$	$N_7(2f^1_{7/2})$	$M\alpha_1$	$M_5 - N_7$

2.2.2 Spectra Assessment

In order to assess qualitatively an EDXRF spectrum, one must comprehend the phenomena contributing to the full extension of the spectrum. In the higher energy region, the elastic and inelastic phenomena take over around 90% of the total number of counts.

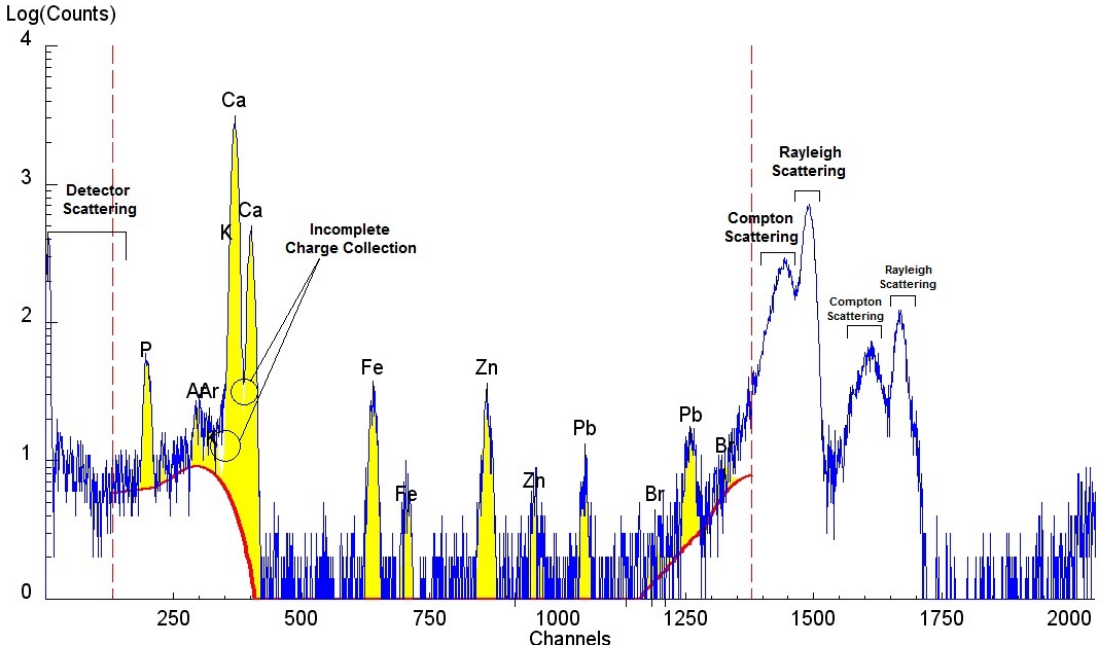

Figure 2.8: Spectra assessment of the reference sample bone ash, using the *WinAxil*© software

We can examine one of the acquired spectra in figure 2.8. The Compton peak's lower intensity (comparatively with the Rayleigh peak) is due to the sample's constitution being bone, a heavier Z matrix. The Rayleigh peak has a position and width as expected for a normal fluorescence line. On the other hand, the Compton peak is much broader than a normal characteristic line at that energy. This broader structure is a consequence from scattering over a range of angles and Doppler effect [14].
Other artifacts may be generated throughout the detecting process, the most frequent being the incomplete charge collection, the sum peaks, and the escape peaks.

Sum peaks are a particular form of peak pileup and occur when two X-ray photons arrive to the detector nearly simultaneously and cannot be recognized as separate two events. The pulse, therefore, is measured as the sum of two photon energies [14].
With modern pulse-processing electronics, the pileup effects are mostly suppressed, and the sum peaks are only found when a few large peaks at lower energy dominate the spectrum [14].
Escape peaks are a consequence of the escape of Si-K or Ge-K photons of the detector after photoelectric absorption of the intruding X-ray photon around the edge of the detector. Regarding Si detectors, the escape peak has the energy of the original peak minus 1.74

keV which corresponds to the K_α line energy of Si (for Ge is 9.886 keV). These peaks can be corrected in a fairly easy way, if one knows the energy, width, and relative intensity of the escape [14].
The incomplete charge collection leads to a measured signal lowered than expected, which is caused when electron-hole pairs generated by an X-ray are not swept to the electrical contacts or when the incident photon does not deposit all of its energy in the crystal [34]. Such phenomena can be diminished by the use of a collimator that prevents the incident radiation from interacting in the edges of the detector [14].
Other artifacts that might be present in the spectrum, are the "forbiden" lines. They correspond to the emission of dipolar and quadrupolar magnetic radiation, among others, but they are rather harder to observe, due to their low intensity [15].

All of the phenomena described above lead to the degradation of the signal from the detector and ultimately deteriorate the peak-to-background ratio.

2.2.3 Qualitative and Quantitative Analysis

The qualitative analysis of a X-ray spectrum consists in the identification of each line that constitutes it. Depending on the type of study that is being performed, a qualitative analysis may or may not be enough to obtain the necessary results. In the majority of cases, it is necessary to conduct a quantitative analysis in order to identify and characterize the sample. Quantitative analysis is used to obtain information about the relative amount of elements present in the sample in terms of their concentration (in ppm - parts per million or $\mu g.g^{-1}$).
There are several methods to perform a quantitative analysis, and the method should be chosen accordingly with the application. Considering that the main goal is the determination of a single or several elements in an unknown but constant matrix or in a sample with negligible matrix effects, comparative methods should be of choice. If the matrix effects vary within samples and multi-element determination is required, then mathematical methods must be used, such as the influence coefficient correction method and the Fundamental Parameter method [14, 37].
The Fundamental Parameter method is the most commonly used in XRF quantitative analysis. This method allows the calculation of the intensity of fluorescent radiation as a function of the composition of the specimen (weight fractions), the incident spectrum, and the configuration of the spectrometer used. All other variables used are fundamental constants, such as the mass-attenuation coefficients for a given element at a given wavelength, its fluorescence yield and photoionization cross sections [14].
Theoretically, this method enables the calculation of the intensity of fluorescent radiation from a standard sample considering both primary and secondary fluorescence, and it neglects high-order and scattering effects. The emitted characteristic radiation is absorbed by all matrix elements by amounts relative to their mass attenuation coefficients. Depending

on the energy of the primary beam and on the elements in the sample, this radiation can generate additional fluorescence in the element, thus enhancing the sample's signal [18]. Intensity and concentration are related through the following equation:

$$I_{P_i} = I_0 K_i m c_i A_i \tag{2.23}$$

K_i being the calibration factor, I_0 is the primary intensity (incident beam), m is sample's mass per unit area ($g.cm^{-2}$) , c_i is the concentration of the element, i, and A_i the attenuation factor [38], which is given by [18]:

$$A_i = \frac{1 + e^{\left[\frac{\frac{\mu}{\rho}(E_{1,j})}{sin\varphi_1} + \frac{\frac{\mu}{\rho}(E_{i,j})}{sin\varphi_2}\right] m}}{\Sigma_j c_j \left[\frac{\frac{\mu}{\rho}(E_{1,j})}{sin\varphi_1} + \frac{\frac{\mu}{\rho}(E_{i,j})}{sin\varphi_2}\right] m} \tag{2.24}$$

$$\Sigma_j c_j = 1 \tag{2.25}$$

where $\frac{\mu}{\rho}(E_{1,j})$ is the mass attenuation coefficient of the element, j, at the incident energy and $\frac{\mu}{\rho}E_{i,j}$ is the mass attenuation coefficient for element, j, at characteristic energy for element, i, φ_1 and φ_2 are the angles for incoming and emitted radiation from the sample. The calibration factor, K_i, is:

$$K_i = \Omega \varepsilon_i C_i' \omega_i \sigma_{X_i} P_{L->M} \tag{2.26}$$

where ε_i is the efficiency of the detector for element, i, σ_{X_i} is the cross section for producing characteristic radiation of an element, i, Ω the detector solid angle ω_i, is the fluorescent yield for element i, $P_{L->M}$ is the transition probability from level L to M in element, i, and C_i' is the absorption in air and detector window of the characteristic photons of element, i.

If one considers that the attenuation factor does not suffer significant alterations, one can encounter a linear relation between characteristic X-ray line intensity and elemental concentration in equation 2.23. This linear correlation can be attained through matching the matrix of the calibration standards with the unknown specimen under study [39]. This is the foundation for a quantitative method that disregards the matrix effects: the compare method. Due to the nature of the samples used in this dissertation, the compare method is the one that suits better our quantification analysis needs. We will make use of the software package $WinAXIL^{©}$ to perform a fitting and calibration of the spectra and determine the line intensities. Afterwards the calibration lines will be calculated with the OriginLab software and applied to the unknown samples in order to obtain their elemental concentration.

Nonetheless, there are some disadvantages to compare method, the main one being the selection of the calibration standards. This is required to replicate the matrix and the composition of the sample under investigation [21].

2.2.4 Detection Limits, Precision and Accuracy

The suitability of an analytical technique can be measured through its precision, accuracy, and detection limits for each of the elements for a given kind of matrix. This last parameter stands for the lowest statistically significant concentration level that can be determined from the sample's analysis. The concentration of each element is calculated through its characteristic peak's intensity, which involves knowing the average number of total accumulated counts of X-ray photons in a certain Region of Interest (ROI) and the correspondent background counts [40]. Therefore, the EDXRF detection limits (Detection Limits (DL)) can be calculated with the following equation [18]:

$$DL = \frac{3C_i\sqrt{n_B}}{n_P} \tag{2.27}$$

where C_i is the concentration of the element i, n_B is the counting rate for the background and n_P is the counting rate for the corresponding peak.
In any scientific method, precision needs to be taken into account. It basically indicates how close the measured values in an experiment are to each other, hence its consistency. Inconsistencies originating from the repetition of the measurements can be due to random errors, which is a type of observational error.
Another important parameter to consider in data analysis is the accuracy of the scientific method. Accuracy indicates the proximity between the true value and the measured value. In this dissertation, in order to ensure the best accuracy, samples with certified composition and with similar matrices were used to calibrate the quantitative calculations.

3 Experimental Setup

3.1 Instrumentation

In this section, several components of the spectrometer's setup will be described. The fundamental devices used are the X-ray tube and detector, which will be more thoroughly described in the next sections, but there are other important pieces of instrumentation as well.
In order to perform a dosimetry analysis and guaranty radiation safety around the spectrometer, a Thermo Scientific Electronic Personal Dosimeters (EPD)-G Dosimeter was used.
Due to the X-ray tube's high power, when compared to other portable XRF, it's inner cooling system is not enough to keep the tube and power supply in optimal temperature conditions. For monitoring the X-ray tube's temperature, a RS Components Digital Thermometer was placed on the tube's surface. To help cool the tube and the tube's power supply, two Philips desk fans (with 15W) were also used during the spectra acquisition.
With regard to control and stabilization of both current and voltage of the tube, a National Instruments Data Acquisition (DAQ) M series (NI USB-621X) was connected to the power supply and managed through a LabVIEW interface. All of the equipment described above was already available at the Physics Department.

3.1.1 X-ray Tube

The X-ray tube used in the experimental set up was a Oxford Instruments Jupiter 5000 Series, designed for applications with high flux and continuous operations, featuring a stainless steal, lead-lined package and filled with dielectric oil to guarantee X-ray shielding and heat dissipation [41]. The most important specifications are shown in table 3.1.

A technical drawing with all the dimensions of the tube can be found in Appendix 1.

Regarding the X-ray tube's power supply, a Matsusada Precision XR Series was used, and the specifications are shown in table 3.2. The technical drawings of the power supply can be found in Appendix 1, figure A.2.

Table 3.1: Oxford Instruments Jupiter 5000 X-ray Tube Specifications [41]

X-ray Tube Specifications	
Operating Voltage Range	10-50 kV
Maximum Power	50W
Max. Beam Current	1,0 mA
Focal spot size	50 μm, 55 μm
Window material	Be
Window thickness	127 μm
Cone of Illumination	23º
Window diameter	11,43 mm
Target angle	12º
Max. Operating Temperature	55 ºC on case surface
Weigh	1,82 kg

Table 3.2: Matsusada Precision X-ray Power Supply Specifications [42]

X-ray Power Supply Specifications	
Input Voltage	24 V $\pm$10%
Power	50 W To 100 W
Output Voltage	0 to 50 kV
Output Current	1 mA
Operating Temperature	0 ºC to 55 ºC
Weigh	1,82 kg

The equipment described above was already available at the Physics department of FCT-UNL.

3.1.2 Detector

The detector used is a Vortex-EX silicon drift detector with a 50 mm^2 nominal detection area, a 500 μm thickness and a 12.5 μm Be window. The dead layer has a thickness of 100 nm. This detector presents a 133 eV energy resolution at 5.9 keV and 0.25 ms peaking time [11]. The detector is supplied with the electronics box (including a power supply and a digital pulse processor, a vacuum chamber (sealed with a Be window), and the preamplifier box. The Vortex detector package weighs 0.8 kg [43]. This equipment was already available at the Physics department of FCT-UNL, and its technical drawings can be found in Appendix 1, figure A.3.
Generally, the Digital Pulse Processor (DPP) numerically manipulates the signal, usually with the intention to measure, filter, produce, or compress continuous analog signals. The Vortex's DPP processed result is given by the $PI - SpecA©$ software in the shape of a spectrum. In figure 3.1, a schematic of an ideal DPP is shown, providing information on

the functioning of a DPP. The preamplifier produces an output which consists of small pulses. The said pulses are differentiated so that the step voltage can be measured. A low pass filter improves the signal-to-noise ratio, the output pulses are digitized, and a histogram of the pulse heights is stored in memory. The preamplifier signal is digitized directly using a fast Analogue-to-Digital Converter (ADC). This signal is differentiated using a discrete differencing circuit and sent to a low pass filter which integrates the differentiator output. Afterwards, an algorithm is applied to the input. the digital peak detected is used, and this is value sent to the histogram memory [44].

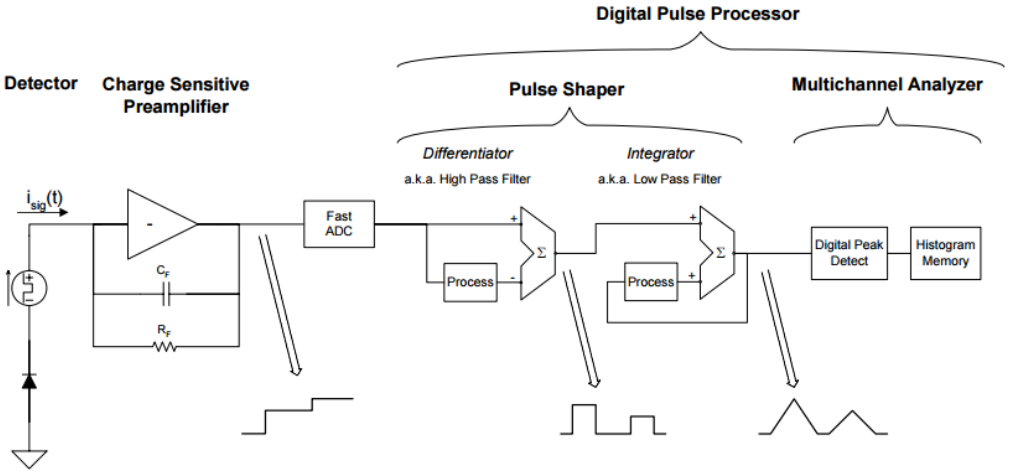

Figure 3.1: Schematic of an ideal DPP [44]

3.1.3 Software

The software employed to acquire data from the detector was the $PI - SpecA^{©}$ software. This receives the voltage, current and acquisition time as inputs, and it allows to overlay two different spectra and to save the data in different formats.

Conductive to the fitting of the spectra acquired with $PI - SpecA^{©}$, the $WinAXIL^{©}$ was the chosen software. This software grants speed and stability of spectrum analysis, reporting capabilities,and provides a powerful environment for spectrum analysis and manipulation [45]. In section 5.3 there is a more detailed exposition on the fitting process with this software. To quantitatively analyze the acquired data, the software $OriginLab^{©}$ was used. Regarding the design of all the components in this dissertation the software $Autodesk^{©}$ Inventor was used.

3.2 Design and Manufacture

3.2.1 Secondary Target

The choice of the secondary target is constrained to the energy region we intend to excite, and the fact that the existing X-ray tube has a Mo (molybdenum, Z = 42, $E_{K\alpha}$ = 17,44 keV) anode.

Considering the X-ray tube's molybdenum anode, it will emit the following radiation energies (apart from the *Bremsstrahlung* and other lower intensity lines):

K_α	K_β	L_α
17,441 keV	19,600 keV	2,293 keV

Given these energies, we were left to choose from Zr (Zirconium, Z = 40, binding energy = 17,99 keV), Y (Yttrium, Z = 39, binding energy = 17,04 keV), Sr (Strontium Z = 38, binding energy = 16,10 keV), Rb (Rubidium, Z = 37, binding energy = 15,20 keV). Due to unavailability of most materials in a pure, sputtering target format, Y was the final choice, allowing ionization of the Yttrium K-shell with both the K_α and K_β lines of Mo.

The yttrium target will emit the following X-ray characteristic radiation:

K_α	K_β	L_α	$L_{\beta 1}$	$L_{\gamma 1}$
14,931 keV	16,731 keV	1,922 keV	1,955 keV	2,346 keV

Due to the L lines low energy, they will show in the spectrum in a low energy narrow region (or will not show at all) not relevant for the type of analyses intended with this spectrometer. Hence, the incoming beam that will interact with our samples is mainly formed by yttrium's K_α and K_β lines.

Table 3.3: Secondary target thickness calculation

ρ_Y [g/cm^3]	Absorption	μ_m[cm^2/g]	$x[cm]$
4,472	99%	10,65	0,096

Table 3.4: Secondary target thickness calculation

Binding Energies [keV]		
Yttrium [Z=39]	Strontium [Z=38]	Rubidium [Z=37]
17,04	16,10	15,20

Given the x value from table 3.3 (calculated with Lambert-Beer law and data from the National Institute of Standards and Technology (NIST) [46], an yttrium target (with less than 1 mm thick absorbs 99% of the incident Mo K_α radiation) was purchased from GoodFellow with the following characteristics:

Purity	Thickness	Diameter
99%	1,0 mm $\pm$15%	25,0 mm$\pm$0,5 mm

Concerning the design of the support for the secondary target, the cone of illumination of the x-ray tube must be taken into account to ensure that the entire beam only interacts

with the secondary target and not it's surroundings to avoid excitation of elements other than the yttrium.

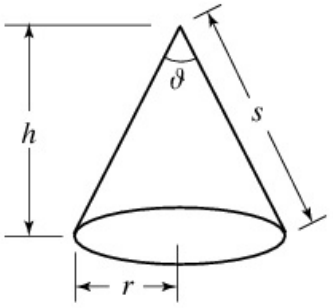

$$\theta = 2 \times tan^{-1}\left(\frac{r}{h}\right) \tag{3.1}$$

Figure 3.2: Cone angle [47]

Using equation 3.1, the tube's provider information about the cone angle, and considering that the tri-axial geometry demands a 45º inclination of the secondary target, we were able to design a proper support. The measures and technical drawing can be found in Appendix 1 (figures A.8 and A.9). Figure 3.3, shows a sketch of the support designed to hold the secondary target in the correct geometry.

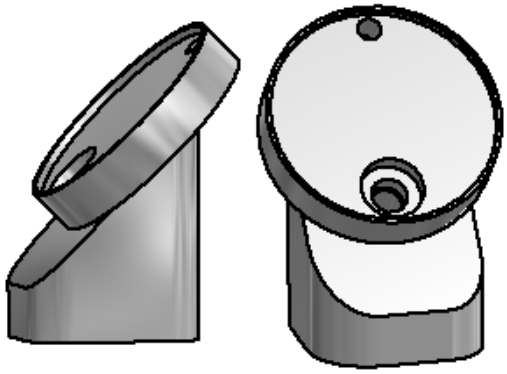

Figure 3.3: Two views of the design of the secondary target's support: technical details in Appendix 1: A.8 and A.9

3.2.2 Collimators

Throughout the data acquisition process, a total of three collimators of two different materials were used. In table 3.6, the sizes and materials of the collimators are shown. Both collimators 1 and 3 had already been purchased by the Physics Department, and collimator 2 was manufactured in the Department's workshop with silver existent in the lab.

Table 3.5 shows the minimum thickness necessary to absorb 99% of the radiation for each collimator's material. Comparing with table 3.5, the collimators already existing in the lab met the minimum requirements to be used effectively in this spectrometer.

In the final set up only two of three collimators were used. Collimator 1 was used

Table 3.5: Silver and Tungsten collimators thickness calculation

Element	ρ [g/cm^3]	Absorption	μ_m[cm^2/g]	$x[cm]$
Ag	10,49	99%	39,98	0,011
W	19,25	99%	138,9	0,002

Table 3.6: Different collimators used in the setup

	Collimators				
	Element	Internal Diameter [mm]	External Diameter [mm]	Length [mm]	Weight [g]
1	Ag	$8 \pm 0,1$	$10 \pm 0,1$	$10 \pm 0,1$	29,8
2	Ag	$2 \pm 0,1$	$15,5 \pm 0,1$	$0,99 \pm 0,1$	2
3	W	$2 \pm 0,1$	$15,5 \pm 0,1$	$1,7 \pm 0,1$	6,7

between the secondary target and the sample, and collimator 2 was allocated between the sample and the detector. The technical drawings for collimator 2 and supports for both collimators can be found in Appendix 1, figure A.4.

3.2.3 Lead Shielding

Due to the hazard that X-ray radiation presents for the spectrometer's operator, there is a need to shield the radiation exiting the tube. This is done through the use of a layer of lead, for this is the best suited material regarding radiation protection. By applying equation 2.5, it is possible to calculate the thickness (x) of the lead shielding necessary to attenuate 99% of the radiation. The results are shown in table 3.7, and a lead shielding tube was built with an approximate thickness of 0,8 mm (thicker than the requirement in table 3.7). In Appendix 1, figure A.7, the technical drawing of the lead shielding is available.

Table 3.7: Lead shielding thickness calculation

ρ_{Pb} [g/cm^3]	Absorption	μ_m[cm^2/g]	$x[cm]$
11,34	99%	14,36	0,028

3.2.4 Dosimetry

During the process of the design of this spectrometer, the undesirable effects of X-ray radiation were taken into account, not only in the spectra itself, but also in the spectrometer's operator. Since continued X-ray exposure can be harmful, dosimetry is needed to study and measure the dose absorbed by ionizing radiation, for monitoring the radiation exposure of individuals, and to design adequate protection.

In dosimetry the mainly used quantity is the absorbed dose, consisting of the energy absorbed per unit mass from any type of ionizing radiation in any target. The previous

unit of this quantity was the rad, defined as 100 erg.g^{-1}, but currently the gray (Gy) is used, J kg^{-1} [48]:

$$1Gy \equiv \frac{1J}{kg} = \frac{10^7 erg}{10^3 g} = 10^4 \frac{erg}{g} = 100rad \tag{3.2}$$

In order to study the effects of radiation on biological tissues and it's protection, the concept of dose equivalent was created. This quantity (H) is defined as the product of the absorbed dose D and a dimensionless quality factor Q, depending on the linear energy transfer LET, and it's given by [48]:

$$H = QD \tag{3.3}$$

When the dose is expressed in Gy, the (SI) unit of dose equivalent is the rem ("roentgen-equivalent-man"). Since 1 Gy=100 rad, 1 Sv = 100 rem.

Within the scope of radiation protection, a concept that embraces an individual's exposure to radiation, the Negligible Individual risk level, was delineated . The National Council on Radiation Protection and Measurements (NCRP) defines the Negligible Individual Dose (NID) without a corresponding risk level, as the effective dose of 0,01 mSv per year [48].

In order to measure the effective dose at the exit of the tube, a calibrated Thermo Scientific dosimeter was placed at approximately 10 cm from the X-ray tube's exit for the duration of 10 minutes. The obtained value corresponded to 7 μSv. Grossly extrapolating this value for the average time of one spectrum acquisition (30 minutes), and considering that for the purpose of this thesis circa 400 spectra were acquired, the total value of the effective dose was 84 mSv. This is a value for extreme conditions, during the acquisition, the tube's exit is always pointing towards the wall or protected with a 0,8 mm thick lead shield. Besides, the tube has it's own inner shielding, and the exit towards the secondary target and collimator are also shielded, as described in section 3.2.3. During all of the measurements, the tube was always turned off whenever there was a need to switch the samples. All of these measures minimize the operator's exposure to radiation, making this device very safe to operate even without external barriers.

According to the U.S. Food and Drug Administration (FDA), the average "effective dose" from natural background radiation is 3 mSv per year in the United States. Regarding diagnostic techniques, the average "effective dose" from a chest X-ray (PA film) is 0.02 mSv, and the effective doses from diagnostic CT procedures are typically estimated to be in the range of 1 to 10 mSv [49], so the total dose from the conditions described above is within the order of magnitude of a CT scan.

Regarding the Portuguese law dose limits, the Decree-Law number 222/2008 from November 17th states that the effective dose limit for exposed workers shall be 100 mSv for a period of five years, provided that the value does not exceed a maximum effective dose of 50 mSv in any single year[50].

Nonetheless, we would like to perform a more thorough study of the effective dose to which an operator at several distances from the X-ray tube, but, due to equipment constraints, we were not able to performed them.

3.2.5 Other Components

Besides the components described above, other supports were necessary to guarantee the stability of the setup and it's geometry. Due to the portability of the spectrometer, it is important to have a base with all the components securely attached to it in order to facilitate it's mobility. A base support for the constituents of the setup was manufactured in acrylic (Appendix 1, figure A.12), as well as a support for the X-ray tube (Appendix A.11) and supports for the detector, shown in figure 3.4 (the corresponding technical drawings can be consulted in Appendix 1, figure A.6).

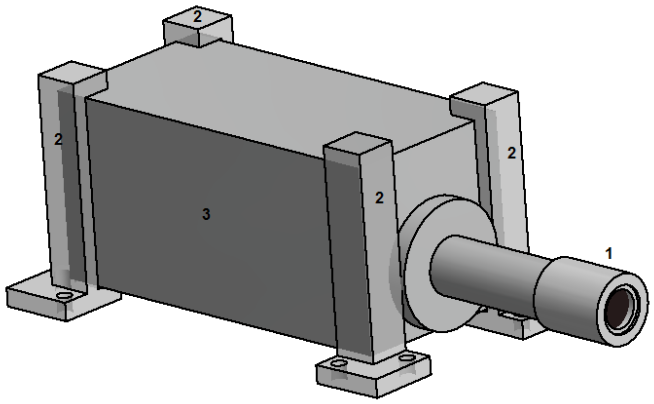

Figure 3.4: Detector and supports: 1 - collimator's support; 2 - acrylic supports; 3 - detector;

To ensure the correct position of the secondary target and the first collimator with the tube, as well as the proper shielding, an aluminum piece was designed in order to align all of these components. Its technical drawing can be consulted in Appendix A, figure A.13. Another acrylic part was design to encompass the aforementioned part and connect it to the setup base support (Appendix 1, figure A.10).

In figures 3.4 and 3.5, it is shown a photograph and a sketch of the designed parts: 1-secondary target support; 2-lead shielding; 3-aluminum support; 4-Silver collimator; 5-Acrylic support.

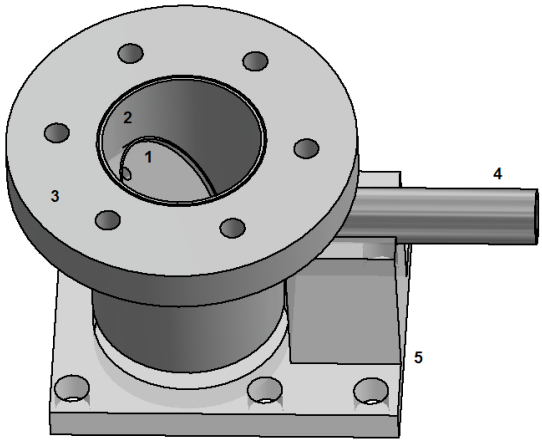

Figure 3.5: Design of the secondary target and collimator support

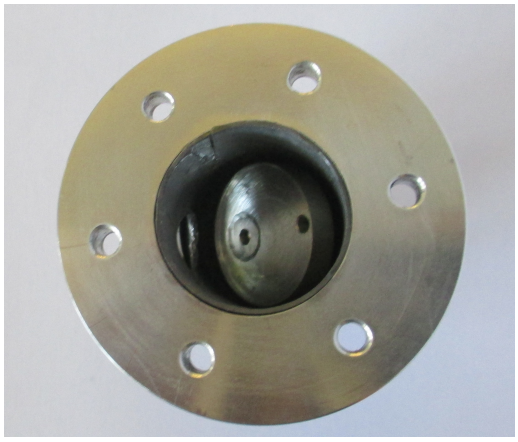

Figure 3.6: Secondary target support's photograph

The whole setup assembly can be see in figures 3.6 and 3.7

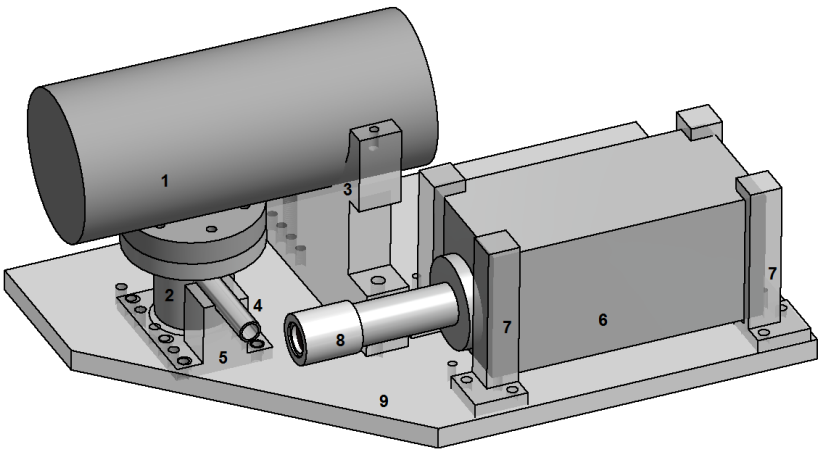

Figure 3.7: Setup's design: 1 - X-ray tube; 2 - secondary target's support; 3 - X-ray tube's support; 4 - Silver collimator; 5 - acrylic support; 6 - detector; 7 - detector's support; 8 - collimator's support; 9 - base support;

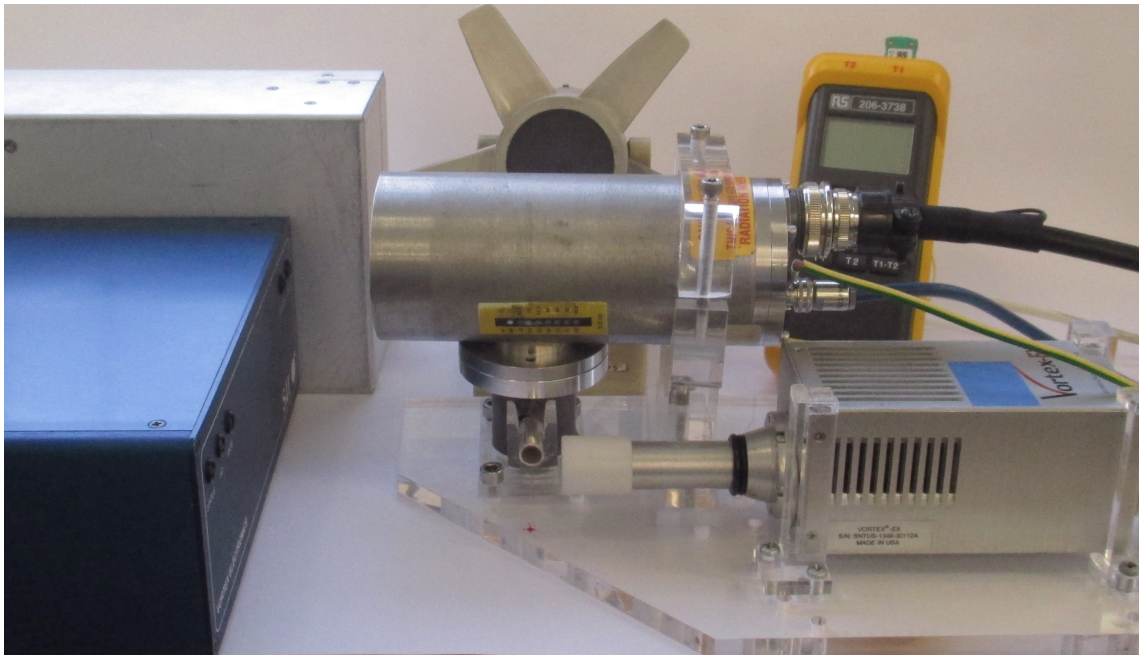

Figure 3.8: Photograph of the setup, along with the temperature sensor, the cooling fan, the X-ray tube power supply and detector's power supply and DPP

3.3 Assembly of the Setup

After gathering all the materials and instruments, the setup was assembled as in figures 3.6 and 3.7. Some small adjustments were needed along the process and were done in the department's workshop. In all of the different setup configurations, the silver collimator (number 1 in table 3.6) was always placed between the secondary target and the sample, and we tested the two other collimators in the nozzle of the detector.

Figure 3.8 shows the resulting spectrum of the orchard leaves (standard reference material NBS-1571) with a tungsten collimator and an aluminum filter (aluminum foil with 0.016 mm thickness) between the secondary target and the silver collimator. Even though the characteristic lines are distinguishable, the peak-background ratio could be improved. In the spectrum, can also be observed molybdenum's Kα line at 17,44 keV, which should not be observed due to the removal of the radiation coming from the X-ray tube due to polarization. This could mean that the radiation might be entering the detector directly without being doubly polarized by the secondary target and the sample.

In figure 3.9, the aluminum filter was removed from the setup, and the collimator at the entrance of the detector was replaced with a silver collimator (number 2 on table 3.6). Removing the filter lowered the background but did not improve the peak-background ratio. The molybdenum problem remained, and the yttrium's Rayleigh peak became more intense than the Compton peak, which should not happen due to the low Z of the orchard leaves matrix. This might indicate that the radiation entering the detector was not coming only from the sample's excitation.

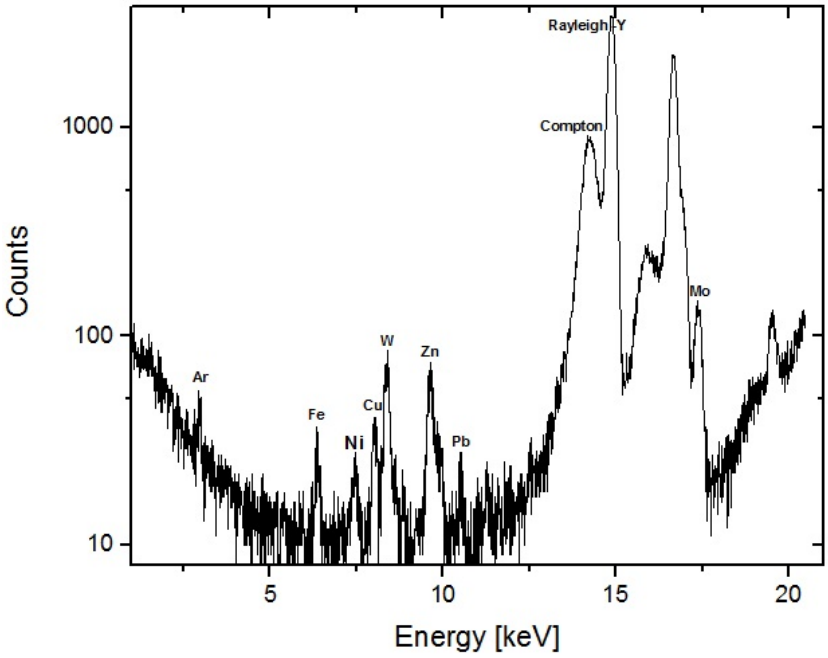

Figure 3.9: Orchard leaves - Setup: Ag collimator after secondary target, W collimator before the detector and Al filter between secondary target and Ag collimator

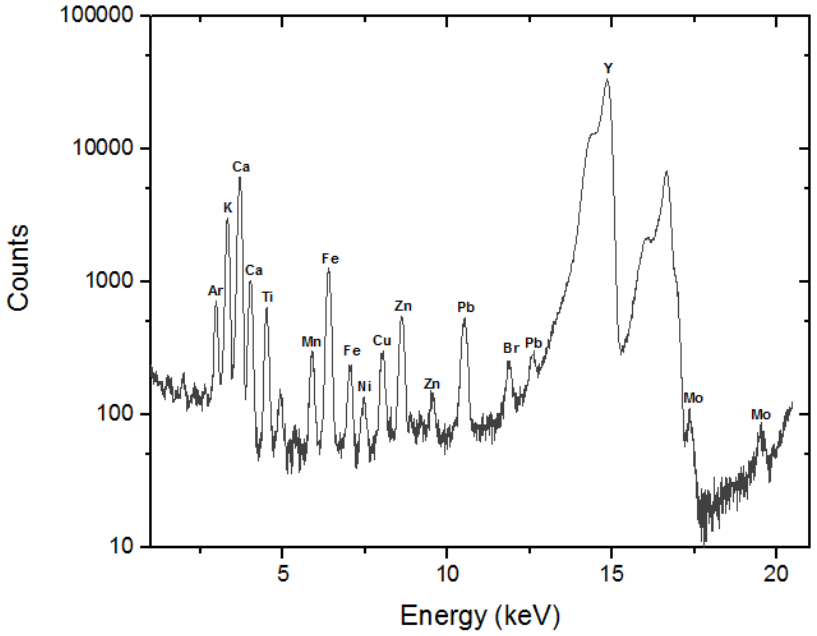

Figure 3.10: Orchard leaves - Setup: Ag collimator after secondary target, Ag collimator before the detector and without Al filter between secondary target and Ag collimator

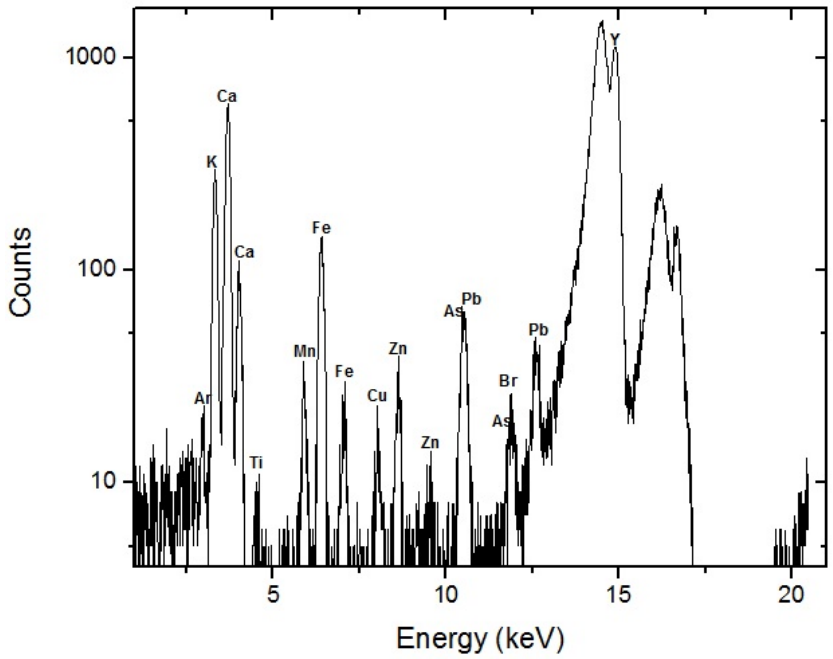

Figure 3.11: Orchard leaves - Setup: Ag collimator after secondary target, Ag collimator before the detector, and extra Pb shielding

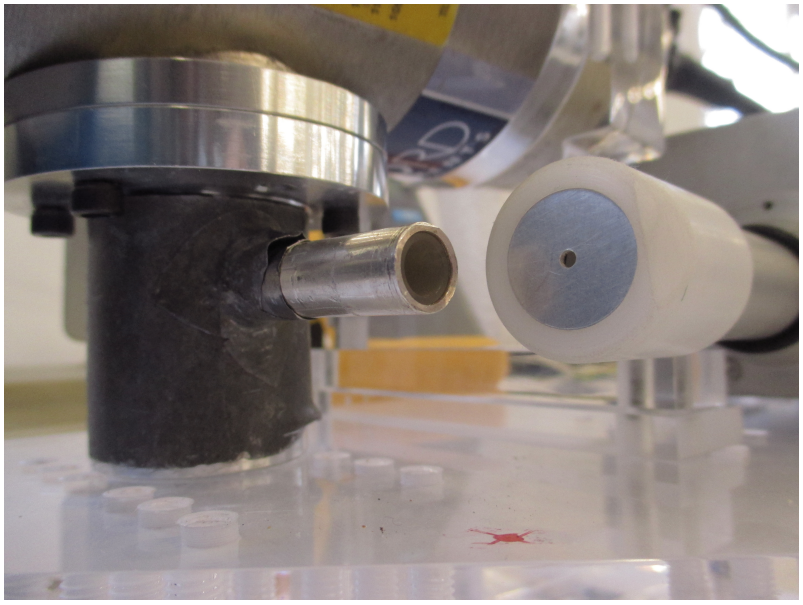

Figure 3.12: Photograph of the added layers of lead shielding

To solve the Rayleigh-Compton issue, we tried to adjust the detector's position, but it was proven that that was not the problem and concluded that non-polarized radiation was coming directly from the tube and exciting the lead in the shielding. This would also explain the molybdenum peak. The most probable cause was the fitting of the collimator tube in the shielding's hole, and this was fixed by adding another lead shielding in the problem area as shown in figure 3.12.

The spectrum shown in figure 3.11 was taken after the lead shielding adjustments were made, and the background reduction is very noticeable, as well as the improvement of the peak-background ratio. The Mo characteristic line is no longer present, and the Compton-Rayleigh ratio is compatible with the sample's low Z matrix.

Henceforward, the setup described above allowed the best results and was the one used throughout the rest of the data acquisition for the samples analyzed in chapter 5.

Shortly after the beginning of the data acquisition with improved setup, the X-ray power supply was broken beyond repair. Fortunately, we were able to borrow the same model of our power supply to finish the measurements within a time constrained period.

3.4 Scattering Spectrum

Initially a diffusion spectrum of a plastic material was acquired to observe the radiation exiting the tube and reaching the sample. One can observe from the diffusion spectra in figure 3.13 that besides the yttrium's characteristic line (at 14,93 keV), the lead's $L\alpha$ line (at 10,55 keV) is also noticeable. This is due to the lead barrier that surrounds the X-ray tube's exit, and it is being excited by the X-rays.

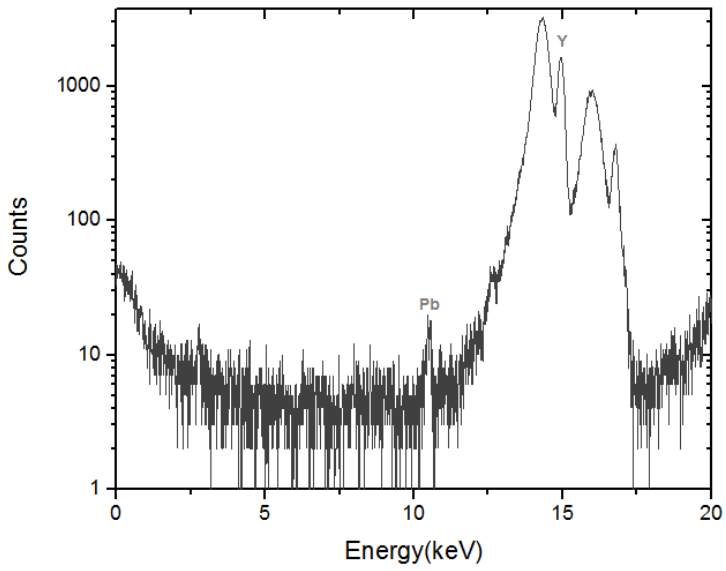

Figure 3.13: Scattering spectrum of plastic

3.5 Bill of Materials

Although most of the instrumentation was already available at the lab and some of the parts were manufactured at the Physics Department workshop without additional costs, the whole project still involved spending, mainly due to the yttrium sputtering target. Table 3.8 shows the costs of the purchased materials for the purpose of this dissertation.

Table 3.8: Total costs of the materials used to assemble the spectrometer

Bill of Materials			
Part	Material	Manufacturer	Cost [€]
8-32 UNC-2B Screws	Inox	Correia Parafusos Lda	6
Collimator + Secondary target's holder	Aluminum	Physics Dep. Workshop	*
Secondary Target holder	Aluminum	Physics Dep. Workshop	*
Collimator	Silver	Physics Dep. Workshop	*
Collimator	Tungsten	Amptek	**
Long Collimator	Silver	GoodFellow	**
Detector's Collimator's Support	Plastic	Physics Dep. Workshop	*
X-ray tube's holder	Acrylic	Acrilfer	8,7 + IVA
Detector's holder	Acrylic	Acrilfer	22,4 + IVA
Structure's holder	Acrylic	Acrilfer	10,5 + IVA
Collimator's holder	Acrylic	Acrilfer	4,5 + IVA
Secondary Target	Yttrium	GoodFellow	425
		Total	477,1 €

*courtesy of the workshop ** previously purchased

4 Experimental Procedure

4.1 Samples

With the purpose to test the spectrometer's potential and to compute it's detection limits and quantification capabilities, two groups of reference material samples were studied: matrices of leaves(orchard leaves NBS-1571, tea leaves GBW 0765, bush branches GBW 07605, and poplar leaves GBW 07604), and bone matrices (caprine bone NYS RM O5-04, bovine bone NYS RM 05-01, bone meal NIST-1486 and bone ash NIST-1400). The reference materials were available in powder and were processed into pellets to be examined with the spectrometer.

Each sample was pressed into pellets with a 15 mm diameter and 1 mm thick without any chemical treatment. A 10 ton pressure was applied for one minute, and each pellet was glued on a Mylar film on a polyester sample holder. Afterwards, the samples were ready to be examined by the spectrometer.

Besides the standard reference materials, other samples were studied. Human remains from the 18th-19th century were investigated, namely the tibia and ribs. In order to be used in a pellet form, it was first necessary to remove a few grams from the inner compact and trabecular area of the bone, with a polyester tool. Afterwards, the collected bone was powdered in a polyester mill and, only then, pressed into a pellet as described earlier [51].

Within the human remains from this period, a femur was also analyzed. The intention was to have samples sharing the same matrix with the bone matrices reference material in order to establish a quantification.

With reference to lighter matrix materials, a paper document from 1779 was also scanned. This document is of particular interest, not only because it was signed by Queen Maria the first of Portugal (the first queen regent) [52], but due to it's rich chemical composition, unusually different from other types of paper from the same period [53].

Lastly, a metal sample was analyzed: a copper alloy disk 40 mm thick and 40 mm in diameter, also a reference standard materials (BCR-691).

4.2 Spectra Acquisition

The spectra acquisition parameters were the following::

- Spectrum Size: 2048 Channels
- Current: 1 mA
- Voltage: 40 kV
- Preset time: 1717 s
- Threshold Energy: 650 eV

Regarding the voltage parameter, we used 40 kV instead of the maximum voltage (50 kV) due to concerns with overheating of the tube and the power supply.

4.3 Spot measurement preparation

In any spectrometer, is important to know the size of the beam's diameter incident in the sample. In order to do so, we exposed an X-ray film in the sample's position to produce a permanent visible radiographic image. After developing the film, the beam's spot can then be evaluated. The latent image formation is due to the ionization of the exposed silver bromide crystals of the film: silver ions are formed on the crystal's surface, and bromine detaches and is absorbed by the gelatin. Only after the developing process thus the image becomes visible. After the five minutes exposure to the X-ray beam, the film was developed in a dark room. Firstly, the film was submerged during two minutes in a mixture of one part water and three parts developer solution. The solution chemically reduces the silver bromide crystals, leading to the precipitation of the silver ions, creating a black area in the radiograph. Afterwards the film was rinsed in a water bath to stop the chemical reaction and then fixated with one part water and one part acidic fixing solution to remove the unexposed and undeveloped silver bromide crystals from the film and harden the emulsion. Finally, the film was washed with water to remove residual chemicals and dried [54].

In order to measure the X-ray spectrometer beam size, or the spot, a radiograph was placed in the same site as the samples. The spot's major axis measured 17 mm, and the minor axis measured 12 mm.

5 Data Analysis

5.1 Standard Spectra

As explained previously in section 4.1, in this dissertation and in order to test the operation of the spectrometer, two groups of standard samples were used to later quantify unknown samples. The first group, made of a lighter matrix, includes orchard leaves, tea leaves, bush branches and poplar leaves, all with known and certified composition. This group should allow the establishment of correlations for similar matrices, such as paper documents. The second group has a slightly heavier matrix and includes bovine and caprine bone, bone meal and bone ash, again, with known and certified composition, that will grant a quantitative correlation with other bone samples.

In this section, we present the spectra used to perform all the data analysis (detection limits and quantification) for each one of the leaves and bone matrices. These spectra were acquired with $PI - SpecA^{©}$ software and were later plotted with the software $OriginLab^{©}$.

5.1.1 Leave's matrices

Figures 5.1 to 5.4 represent the spectra of the four samples of leave's matrices. In all of these spectra, the region of interest (ROI) begins at 2 keV. The Compton peak, located at 14,2 keV, is also noticeably more intense than the yttrium's Rayleigh peak, at 14,9 keV. This is due to the composition of the matrix being essentially made of light elements such as C, O and N, to which the point of balance between Rayleigh and Compton scattering decreases to 10 keV. For heavy elements, like lead, it increases to 150 keV [19].

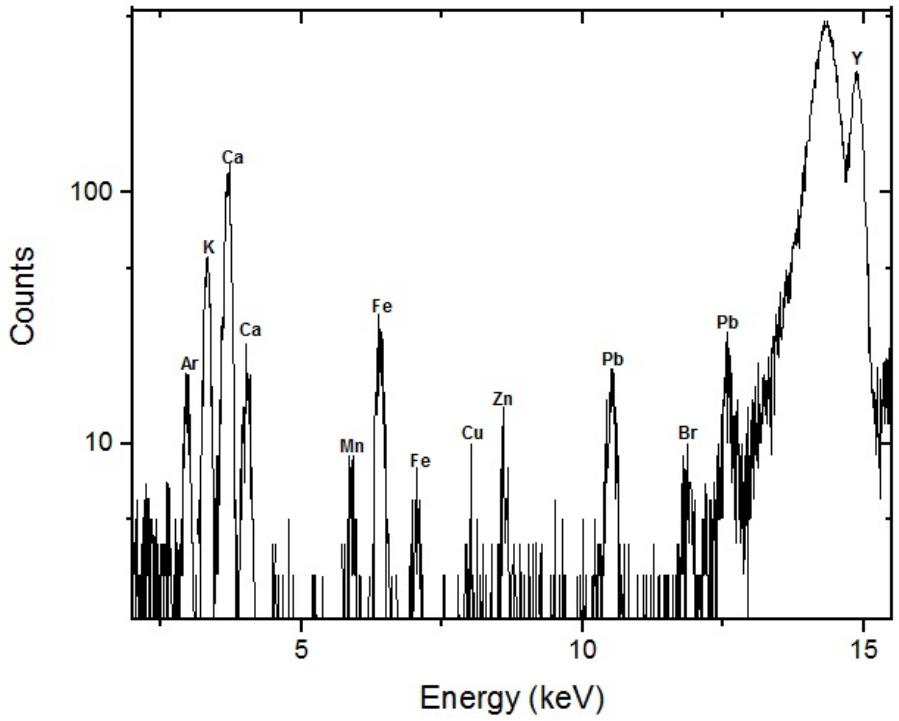

Figure 5.1: Orchard Leaves standard (NBS-1571) pellet spectrum

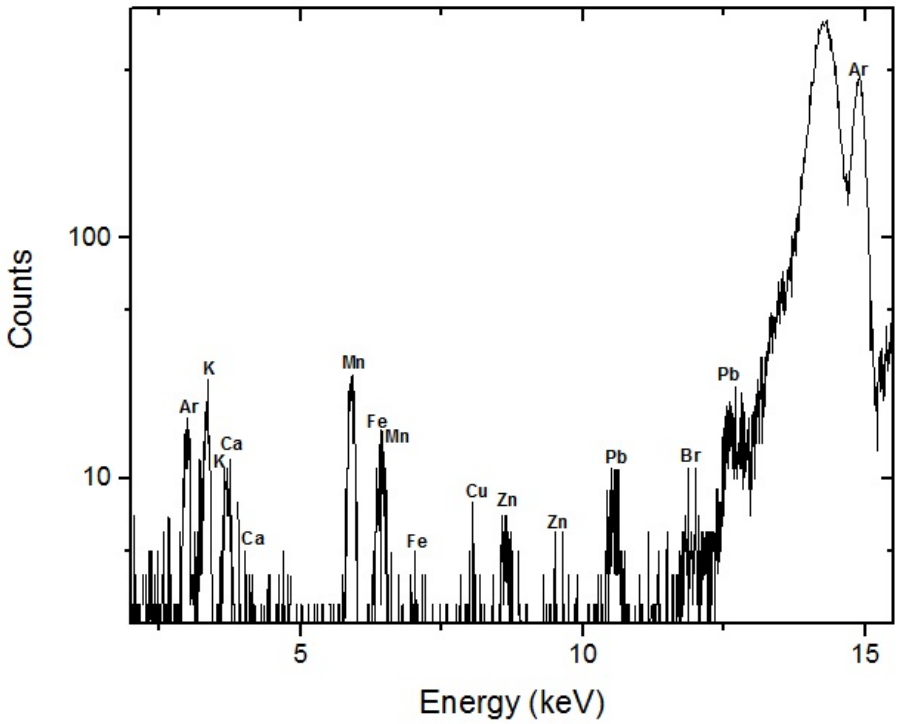

Figure 5.2: Tea Leaves standard (GBW 0765) pellet spectrum

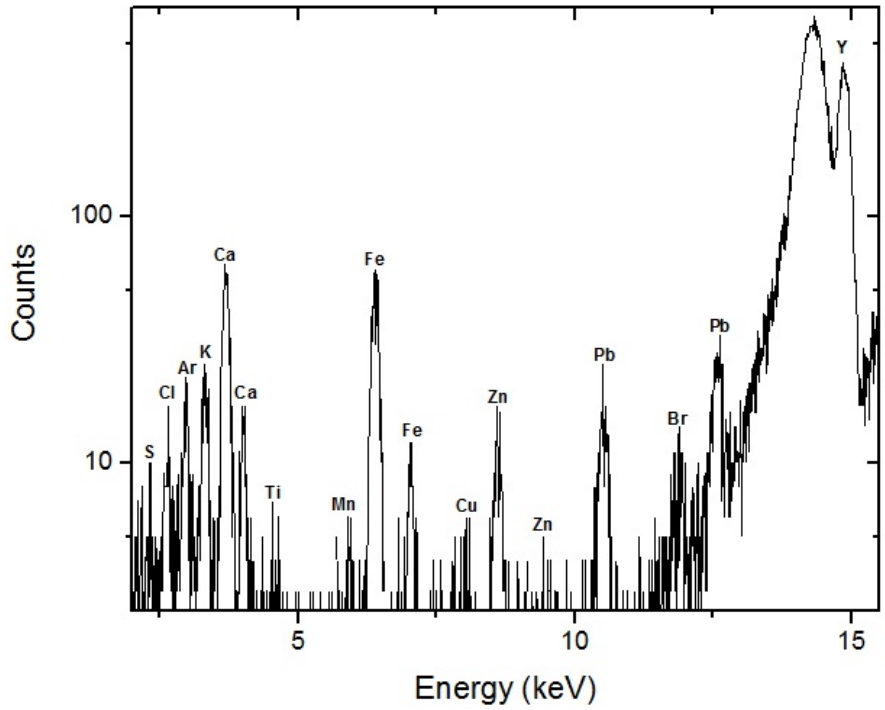

Figure 5.3: Bush Branches standard (GBW 07605) pellet spectrum

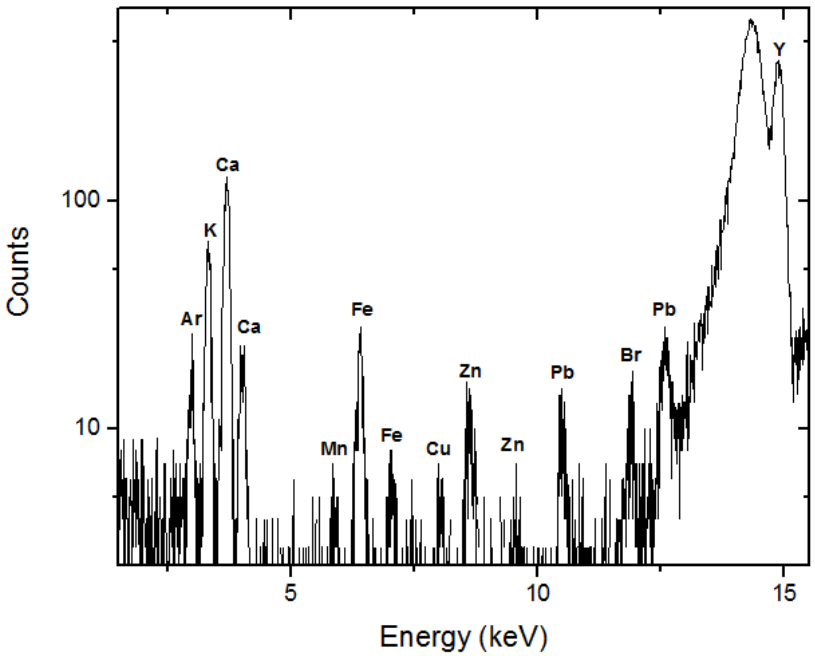

Figure 5.4: Poplar leaves standard (GBW 07604) pellet spectrum

5.1.2 Bone matrix

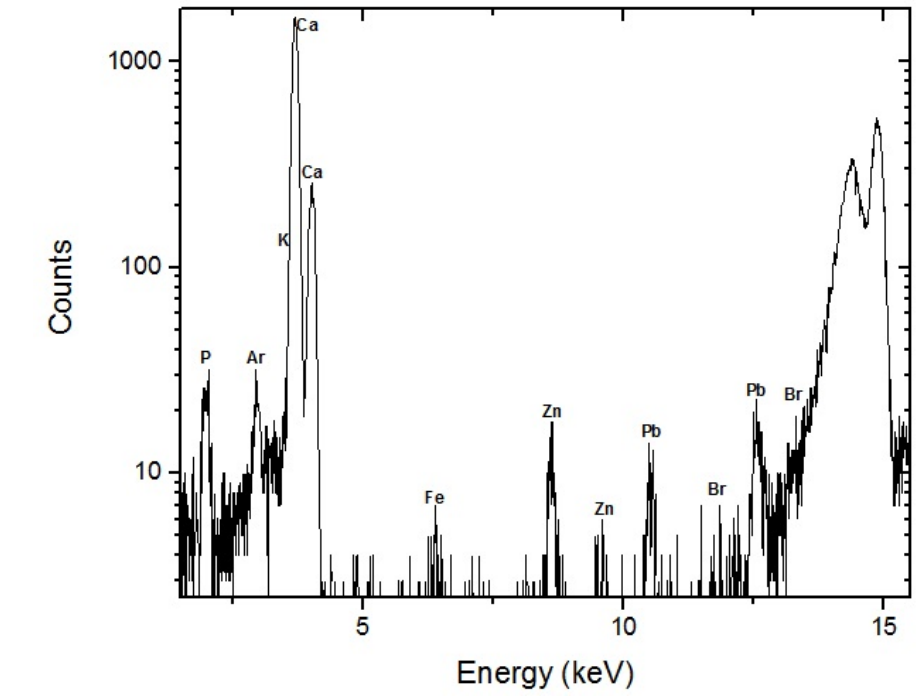

Figure 5.5: Caprine Bone standard (NYS RM O5-04) pellet spectrum

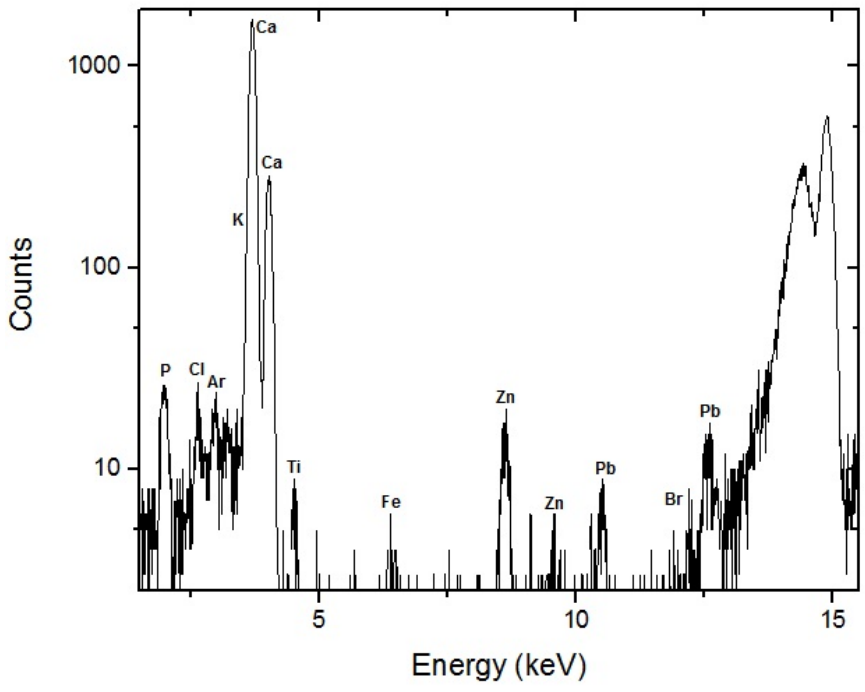

Figure 5.6: Bovine Bone standard (NYS RM 05-01) pellet spectrum

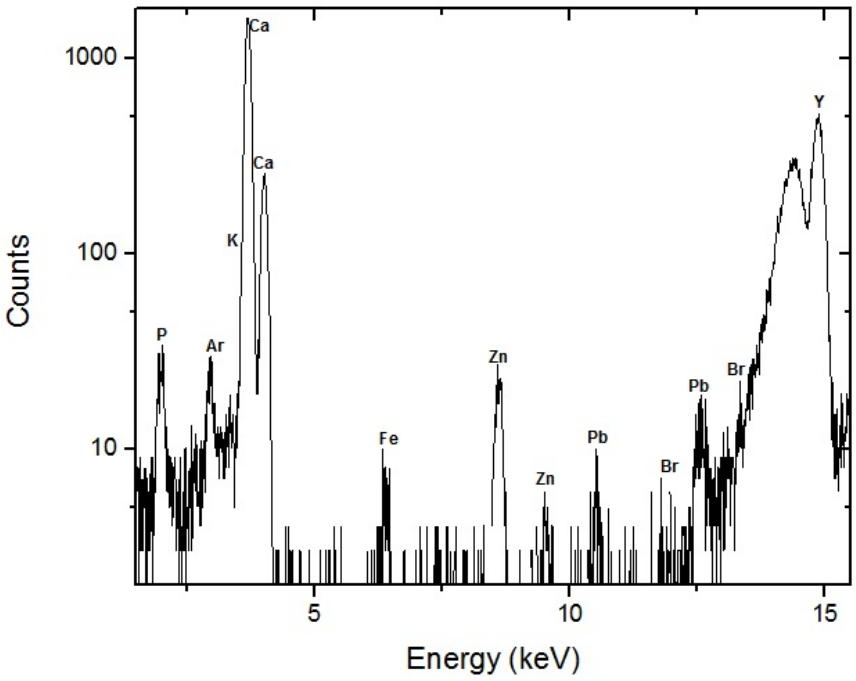

Figure 5.7: Bone Meal standard (NIST 1486) pellet spectrum

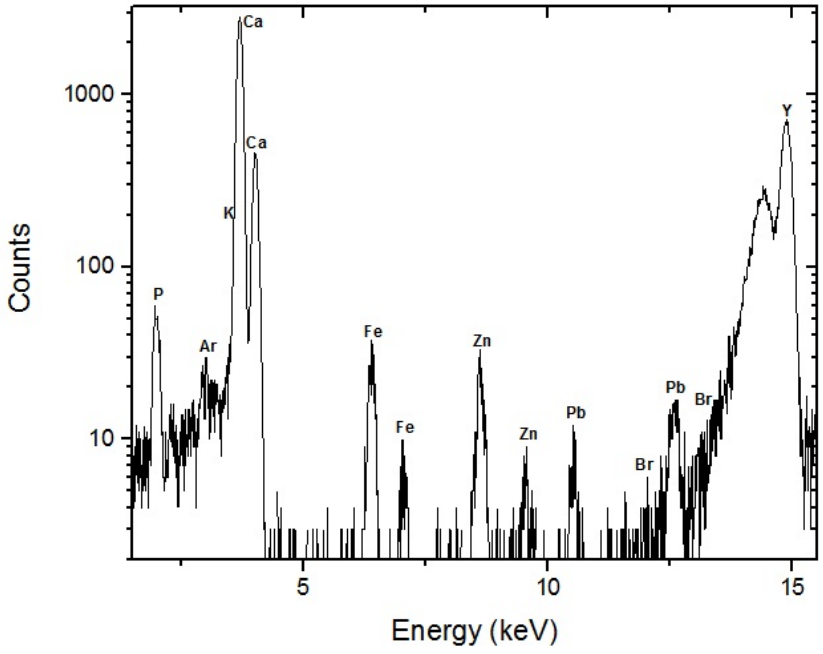

Figure 5.8: Bone Ash standard (NIST 1400) pellet spectrum

Figures 5.5 to 5.8 represent the spectra of the four samples of bone matrices. In all of these spectra, again, the region of interest (ROI) usually starts at 2 keV. However, due to the bone matrix being heavier composition made up of calcium hydroxyapatite $Ca_{10}(PO_4)_6(OH)_2$ (composite material that incorporates calcium phosphate) [55], the yttrium's Rayleigh peak is more intense than the Compton peak.

5.2 Fitting

For the sake of extracting information about the characteristic lines after acquiring and saving the spectra with the $PI - SpecA$©, the spectra was analyzed with $Winaxil$© software. This software receives as input the spectra data and the measurement conditions, such as voltage, current, acquisition time, type of detector, and X-ray source. Afterwards, the calibration is done manually, and the chemical elements are selected according to the elements known to be present in the standard samples within a ROI previously chosen.

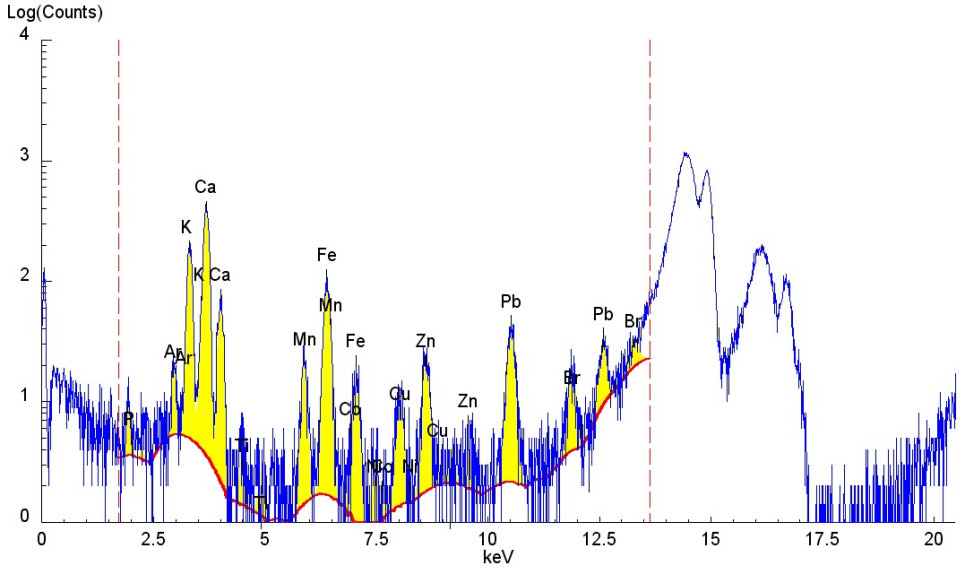

Figure 5.9: Fitting with $Winaxil$© software for the Orchard Leaves standard(NBS-1571) pellet

Thereupon, the software performs a fitting to the selected spectral lines, represented as the yellow area in figure 5.9, with the ROI limited by the dashed red lines. The red line along the spectra establishes the limits between the characteristic peaks and the background. Lastly, $WinAXIL$© produces a text file (called "full report") indicating each element spectral line's area, background, and corresponding uncertainties. This is the information that allows us to perform data analysis such as detection limits calculation, and quantification.

5.3 Detection Limits

The detection limits were calculated by applying the standard sample's certified concentration and the peak and background value given by the $Winaxil$© software to equation 2.27.

In order to calculate the error associated with the detection limits calculation, we applied the propagation of uncertainty law, which determines the effect of variables' uncertainties on the uncertainty of a function based on them [56]. Since both concentration,

Table 5.1: Detection Limits ($\mu g.g^{-1}$) for standard materials: poplar leaves (GBW 07604) and bone ash (NIST 1400).

Detection Limits [$\mu g.g^{-1}$]		
Element	Poplar Leaves	Bone Ash
Ca	$16 \times 10^1 \pm 3 \times 10^1$	$33 \times 10^1 \pm 4 \times 10^1$
K	$0,6 \times 10^1 \pm 0,1 \times 10^1$	$8 \times 10^1 \pm 3 \times 10^1$
Zn	$0,3 \times 10^1 \pm 0,1 \times 10^1$	$0,9 \times 10^1 \pm 0,1 \times 10^1$
Fe	$0,8 \times 10^1 \pm 0,1 \times 10^1$	$1,4 \times 10^1 \pm 1 \times 10^1$
Pb	$0,1 \times 10^1 \pm 0,1 \times 10^1$	$0,1 \times 10^1 \pm 0,1 \times 10^1$
Br	$0,2 \times 10^1 \pm 0,1 \times 10^1$	
Mn	$1 \times 10^1 \pm 0,3 \times 10^1$	

and peak and background areas have associated errors, these errors will propagate and can be calculated by the following:

$$\frac{u(D.L.)}{D.L.} = \sqrt[2]{\left(\frac{u(C)}{C}\right)^2 + \left(\frac{u(N_p)}{N_p}\right)^2 + \left(\frac{u(N_b)}{N_b}\right)^2} \tag{5.1}$$

where u is the variable's uncertainty, D.L. stands for detection limits, N_p is the characteristic peak area for said element, and N_b is the corresponding background.

In table 5.1, the detection limits can be observed for one of the leaf matrices (poplar leaves) and one for the bone matrices (bone ash), with the respective errors.

Following the calculation of the detection limits, we aim to compare these values with the detection limits obtained using different XRF setups.
Firstly, we will compare with the results obtained for the bench top tri-axial spectrometer in "Comparison of matrix effects on portable and stationary XRF spectrometers for cultural heritage samples [10]" for three reference materials: orchard leaves (NBS-1571), bone ash (NIST-1400) and copper alloy (BCR-691).
The bench top spectrometer used is a commercial X-ray tube (Philips, PW 1140; 100 kV, 80 mA) with a molybdenum secondary target. The X-ray tube, the secondary target, and the sample are also in a tri-axial geometry. The beam is collimated throughout two silver apertures before and after the secondary target. The distance between the sample and the detector is 27 mm, and the incident X-ray spot has an elliptic form with a horizontal axis of approximately 20 mm and a vertical axis of approximately 15 mm. The detector used is Si(Li) with a 30 mm^2 active area and 8 μm beryllium window. The operating conditions of this system were 50 kV and 20 mA [10].

From table 5.2, one realizes that there are elements on lighter matrices, such as orchard leaves, that are only detected by the bench top spectrometer. For medium Z matrices, like bone ash, the same elements are detected by both setups. In heavy matrices, like copper alloy, elements like iron (Fe) and nickel (Ni) are detected by the portable spectrometer and

Table 5.2: Detection Limits ($\mu g.g^{-1}$) comparison with a bench top spectrometer (adapted from[10]) for standard materials: orchard leaves (NBS-1571) and bone ash (NIST 1400).

	Detection Limits [$\mu g.g^{-1}$]		
	Portable tri-axial		
	Orchard Leaves	Bone Ash	Copper Alloy
K	$3,4 \times 10^2 \pm 0,4 \times 10^2$	$7,5 \times 10^1 \pm 2 \times 10^1$	-
Ca	$2,1 \times 10^2 \pm 0,2 \times 10^2$	$3,2 \times 10^2 \pm 0,3 \times 10^2$	-
Mn	$1,3 \times 10^1 \pm 0,2 \times 10^1$	-	-
Fe	$0,9 \times 10^1 \pm 0,1 \times 10^1$	$1,4 \times 10^1 \pm 0,2 \times 10^1$	$1,9 \times 10^1 \pm 0,3 \times 10^1$
Ni	-	-	$2,3 \times 10^2 \pm 0,4 \times 10^2$
Cu	-	-	-
Zn	$0,4 \times 10^1 \pm 0,1 \times 10^1$	$0,8 \times 10^1 \pm 0,1 \times 10^1$	$2 \times 10^2 \pm 0,2 \times 10^2$
As	-	-	$3 \times 10^1 \pm 0,3 \times 10^1$
Br	$0,6 \times 10^1 \pm 0,1 \times 10^1$	-	-
Rb	-	-	-
Sr	-	-	-
Sn	-	-	$37 \times 10^2 \pm 5 \times 10^2$
Pb	$0,6 \times 10^1 \pm 0,1 \times 10^1$	$0,1 \times 10^1 \pm 0,1 \times 10^1$	$3,3 \times 10^2 \pm 0,5 \times 10^2$
	Bench top		
	Orchard Leaves	Bone Ash	Copper Alloy
K	6×10^1	$4,7 \times 10^1$	-
Ca	$3,5 \times 10^1$	$7,4 \times 10^1$	-
Mn	$0,3 \times 10^1$		-
Fe	$0,2 \times 10^1$	$0,5 \times 10^1$	-
Ni	$0,1 \times 10^1$	-	-
Cu	$0,1 \times 10^1$	-	-
Zn	$0,1 \times 10^1$	$0,3 \times 10^1$	6×10^1
As	$0,1 \times 10^1$	-	4×10^1
Br	$0,1 \times 10^1$	-	-
Rb	$0,1 \times 10^1$	-	-
Sr	$0,1 \times 10^1$	$0,1 \times 10^1$	-
Sn	-	-	$16,35 \times 10^2$
Pb	$0,1 \times 10^1$	$0,2 \times 10^1$	$5,4 \times 10^1$

not detected by the bench top.

Notwithstanding, a comparison can be made between both setups, for the values are within the same order of magnitude. We were able to identify more elements of the alloy using the portable configuration, making this spectrometer more suitable for higher Z elements. Overall, the detection limits are better for the bench top spectrometer, which was to be expected, mostly due to the use of a more powerful X-ray tube, but both perform similarly in identifying the elemental composition of the samples.

Another comparison was made with a portable planar spectrometer with 90^{o} geometry [11], using the same detector used in this dissertation setup and a low power X-ray tube. For this comparison, two reference materials were used: orchard leaves (NBS-1571) and bone meal (NIST-1486). The spectrometer used for the comparison is an Eclipse IV Amptek X-ray tube (45 kV 50 mA) with a Rh anode, with a 5 mm beam diameter after collimation through a tantalum collimator. The sample is 55 mm from tube's Be window and 10 mm from the detector's Be window. The acquisition time was 1800 seconds, and the detector was a Vortex SDD with a 50 nominal detection area and 500 μm thickness and a 12.5 μm Be window. The dead layer has a thickness of 100 nm and a 133 eV energy resolution at 5.9 keV and 0.25 ms peaking time [11].

The detection limits attained for both set ups are shown in table 5.3. For lighter matrices, like the orchard leaves, the planar spectrometer performs better, for it is able to identify more elements. This is due to Rh anode of tube in comparison with the Mo anode and Y secondary target in the tri-axial, for it will not excite lighter elements (with lower energies and lower ionization cross-section), which is also the reason for the disparity in resolution for elements like Ca and K. Regarding medium matrices such as the bone ones, both setup performs similarly, and apart from P, the tri-axial reaches better detection limits.

Table 5.3: Detection Limits ($\mu g.g^{-1}$) comparison with Vortex SDD detector for a portable 90º geometry spectrometer (adapted from[11]), for standard materials: orchard leaves (NBS-1571) and bone meal (NIST-1486)

Detection Limits [$\mu g.g^{-1}$]		
	Portable tri-axial	
	Orchard Leaves	Bone Meal
P	-	$21 \times 10^3 \pm 5 \times 10^3$
S	-	-
Cl	-	-
K	$3,5 \times 10^2 \pm 0,4 \times 10^2$	$8,6 \times 10^1 \pm 2 \times 10^1$
Ca	$2,2 \times 10^2 \pm 0,2 \times 10^2$	$2,3 \times 10^2 \pm 0,3 \times 10^2$
Mn	$1,3 \times 10^1 \pm 0,2 \times 10^1$	-
Fe	$0,9 \times 10^1 \pm 0,1 \times 10^1$	$0,9 \times 10^1 \pm 0,3 \times 10^1$
Cu	-	-
Zn	$0,4 \times 10^1 \pm 0,1 \times 10^1$	$0,7 \times 10^1 \pm 0,2 \times 10^1$
Br	$0,6 \times 10^1 \pm 0,1 \times 10^1$	-
Sr	-	-
Pb	$0,2 \times 10^1 \pm 0,1 \times 10^1$	$0,1 \times 10^1 \pm 0,1 \times 10^1$
	Portable 90º	
	Orchard Leaves	Bone Meal
P	$5,12 \times 10^2 \pm 0,4 \times 10^2$	$28,92 \times 10^2 \pm 0,5 \times 10^2$
S	$8,2 \times 10^2 \pm 1 \times 10^2$	-
Cl	$2 \times 10^2 \pm 0,2 \times 10^2$	-
K	$2,74 \times 10^2 \pm 0,06 \times 10^2$	-
Ca	$1,41 \times 10^2 \pm 0,02 \times 10^2$	$3,12 \times 10^2 \pm 0,03 \times 10^2$
Mn	$1,2 \times 10^1 \pm 0,1 \times 10^1$	-
Fe	$1,2 \times 10^1 \pm 0,1 \times 10^1$	$1,7 \times 10^1 \pm 0,1 \times 10^1$
Cu	$0,1 \times 10^1 \pm 0,1 \times 10^1$	-
Zn	$0,2 \times 10^1 \pm 0,1 \times 10^1$	$1,2 \times 10^1 \pm 0,1 \times 10^1$
Br	-	-
Sr	-	$5,4 \times 10^1 \pm 0,2 \times 10^1$
Pb	-	-

5.4 Quantification

Concerning the quantitative analysis, as it was explained in section 2.2.3, due to the nature of the samples, compare mode will be used to perform the samples quantification, over the fundamental parameter method. The reference materials that we decided to use to quantify unknown samples share similar matrices and dimensions, meaning that the K_i, attenuation factor does not suffer significant variations within the same matrix group. Consequentially, according to equation 2.3, a linear relation between characteristic X-ray line intensity and elemental concentration is expected. So, the quantification of elements for each type of matrix (leaves and bones), was achieved through plotting the element certified concentration versus that same element's characteristic peak area (as in figure 5.10), for each reference material. The linear equation attained from this plot (y=mx+b) is applied to the unknown sample's element characteristic line area (available on the full report produce by $WinAxil^{©}$), calculating its correspondent concentration value. And this is done for all the elements that can be quantified through this method.

Thus, we were able to quantify Ca, K, Fe, Zn, Pb, Br and Mn for the leaves matrices, and we quantified Ca, P, K, Fe, Zn and Pb for the bone matrices. Regarding the quantification of Pb, even though is evident in figure 3.13 that the spectral line for lead is overvalued, this consists of a systematic error, and it is present in both reference samples as well as other analyzed samples. Therefore, it does not affect the final value of the Pb concentration, which is quite accurate, as it can be observed in table 5.4.

Afterwards, there is the need to calculate the uncertainty associated with the quantification calculation. Not only the certified concentration and the area values have affiliated uncertainties, the equation's slope (m) and intercept (b) also have uncertainties to be taken into account. To determine the concentration's uncertainty we will graphically determine the ranges of possible values of m and b, by drawing the lines of maximum slope and minimal slope that are still representative of the values within the error bars [56], as represented in figure 5.10.

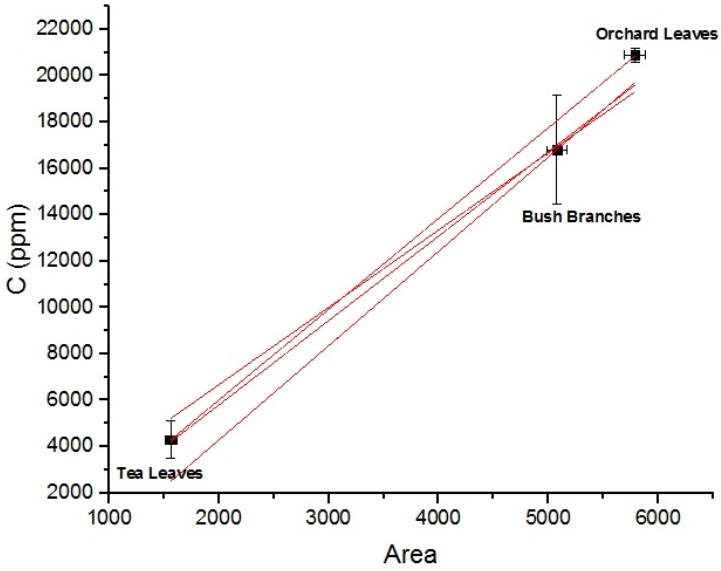

Figure 5.10: Graphic uncertainty calculation for Ca quantification in the leaves matrices

5.5 Accuracy

One of the most important aspects in a quantitative analyses is to ensure its accuracy. As described in section 2.2.4, accuracy indicates the proximity between the true value and the measured value. To test the accuracy of our quantification, six samples with certified composition from two types of matrices were used. The first group, leaves matrix, is compared in table 5.4, in which the "Reference" column indicates the certified value of the samples, and the "Obtained" value indicates the value obtained with our experimental setup after applying the data treatment described in the previous sections.

We can observe that most of the elements that we were able to quantify, have similar and proportional concentrations. Almost all of the elements calibrated show great agreeableness with the reference values, which demonstrates the quality of this method. Regarding the lead's concentrations in the tea leaves sample, it's concentration value differs from the reference value for two possible reasons. Firstly, the reference concentration is very low, bellow the spectrometer's detection limit for lead. Secondly, due to the lead peak present in the scattering spectra (figure 3.13). We suspect that the lead shielding around the tube's nozzle is being excited, hence the peak at 10,5 keV in the diffusion spectra, which causes the lead concentration to always be higher than the actual lead's content of the sample, so this is an expected effect. Regarding the lead's concentration in the orchard leaves sample, the value is quite accurate, because the actual concentration is now detectable with by our spectrometer.

Regarding the second group of samples, the bone matrix one, results are shown in table 5.5. Similarly to the leaves matrix, most of the elements' concentration show great affability with the reference concentrations. Concerning the lead's concentration values for the mone meal samples, the explanation stands the same: the values obtained are higher

Table 5.4: Accuracy of the scientific method for the reference samples with leaves matrices

Accuracy - Concentrations		
	Tea Leaves - GBW 0765	
	Reference $[\mu g.g^{-1}]$	Obtained $[\mu g.g^{-1}]$
Ca	$4,3 \times 10^3 \pm 0,8 \times 10^3$	$4,9 \times 10^3 \pm 0,4 \times 10^3$
K	$1,66 \times 10^4 \pm 0,2 \times 10^4$	$1,8 \times 10^4 \pm 0,5 \times 10^4$
Fe	$2,64 \times 10^2 \pm 0,3 \times 10^2$	$3,7 \times 10^2 \pm 0,3 \times 10^2$
Zn	$2,6 \times 10^1 \pm 0,4 \times 10^1$	$3,6 \times 10^1 \pm 0,4 \times 10^1$
Pb	$0,44 \times 10^1 \pm 0,06 \times 10^1$	$2,2 \times 10^1 \pm 0,3 \times 10^1$
Br	$0,34 \times 10^1 \pm 0,1 \times 10^1$	$0,27 \times 10^1 \pm 0,1 \times 10^1$
	Orchard Leaves NBS-1571	
	Reference $[\mu g.g^{-1}]$	Obtained $[\mu g.g^{-1}]$
Ca	$20,9 \times 10^3 \pm 0,3 \times 10^3$	$18,2 \times 10^3 \pm 0,9 \times 10^3$
K	$14,7 \times 10^3 \pm 0,3 \times 10^3$	$12,4 \times 10^3 \pm 1 \times 10^3$
Fe	$3 \times 10^2 \pm 0,2 \times 10^2$	$2,9 \times 10^2 \pm 0,4 \times 10^2$
Zn	$2,5 \times 10^1 \pm 0,3 \times 10^1$	$2,1 \times 10^1 \pm 0,4 \times 10^1$
Pb	$4,4 \times 10^1 \pm 0,44 \times 10^1$	$4,9 \times 10^1 \pm 0,7 \times 10^1$
Br	$1 \times 10^1 \pm 0,1 \times 10^1$	$0,4 \times 10^1 \pm 0,1 \times 10^1$
Mn	$9,1 \times 10^1 \pm 0,4 \times 10^1$	$7,8 \times 10^1 \pm 0,9 \times 10^1$

Table 5.5: Accuracy of the scientific method for the reference samples with bone matrices

Accuracy - Concentrations		
	Bone Meal - NIST 1486	
	Reference $[\mu g.g^{-1}]$	Obtained $[\mu g.g^{-1}]$
Ca	$26,6 \times 10^4 \pm 0,2 \times 10^4$	$26,02 \times 10^4 \pm 1 \times 10^4$
P	$12,3 \times 10^4 \pm 1 \times 10^4$	$12,3 \times 10^4 \pm 4 \times 10^4$
K	$41,2 \times 10^1 \pm 0,4 \times 10^1$	$3,4 \times 10^2 \pm 1 \times 10^2$
Fe	$9,9 \times 10^1 \pm 0,8 \times 10^1$	$1,4 \times 10^2 \pm 1 \times 10^2$
Zn	$14,7 \times 10^1 \pm 1 \times 10^1$	$14,6 \times 10^1 \pm 0,2 \times 10^1$
Pb	$0,13 \times 10^1 \pm 0,01 \times 10^1$	$1,5 \times 10^1 \pm 0,4 \times 10^1$

due to concentration being inferior to the detection limit, and the excitation of the lead in the shielding. Overall, the quantitative method employed proved to be quiet accurate, considering the values discussed above.

5.6 Case studies

In this section we will analyze several bone samples from human remains of the 18th century and a paper document from 1779. All the samples spectra will be presented, and

bone quantification will be compared with a bench top XRF tri-axial spectrometer obtained values. The document's spectrum will be qualitatively evaluated and compared with a spectrum retrieved with a portable planar 90º geometry spectrometer.

5.6.1 Analysis of human bone remains from the 18th century

As previously mentioned, in this section we will analyze the quantification and spectra of three pellet samples: rib and tibia from individual 54. The femur (EES-E8A3C) spectra will also be evaluated.

The compare mode quantitative method was applied to samples of unknown composition: rib and tibia pellets from individual 54, skull pellet from individual 31 and a femur (EES-E8A3C). Table 5.6 shows the results of the quantification.

Table 5.6: Quantitative calculation: Concentration $mg.g^{-1}$ of human remains from the 18th century: rib, tibia (individual 54), and femur (EES-E8A3C)

	Concentration $[\mu g.g^{-1}]$		
	Ribs	Femur	Tibia
Ca	$36,2 \times 10^4 \pm 0,6 \times 10^4$	$7,9 \times 10^4 \pm 0,3 \times 10^4$	$28,8 \times 10^4 \pm 0,7 \times 10^4$
K	$4 \times 10^2 \pm 0,8 \times 10^2$	$3 \times 10^2 \pm 0,9 \times 10^2$	$3 \times 10^2 \pm 2 \times 10^2$
Fe	$6,6 \times 10^3 \pm 0,3 \times 10^3$	$2,7 \times 10^3 \pm 0,3 \times 10^3$	$4,9 \times 10^2 \pm 0,9 \times 10^2$
Zn	$5,9 \times 10^2 \pm 0,3 \times 10^2$	$10 \times 10^2 \pm 0,7 \times 10^2$	$1,4 \times 10^2 \pm 0,2 \times 10^2$
Pb	$2,8 \times 10^2 \pm 0,3 \times 10^2$	$7 \times 10^1 \pm 1 \times 10^1$	$8 \times 10^1 \pm 2 \times 10^1$
Br	$3,8 \times 10^2 \pm 0,5 \times 10^2$	$8 \times 10^1 \pm 3 \times 10^1$	$4 \times 10^1 \pm 2 \times 10^1$

Figure 5.11 shows the spectrum obtained for the rib pellet, with a region of interest between 2keV to 13keV.As expected from a bone material, the Ca $K\alpha$ (3,69keV) and $K\beta$ (4,01keV) has the highest intensity (and peak area) for this is one of the main constituents in bones. We were also able to detect elements present in the bone matrices reference materials, such as P, K, Fe, ad Zn.

Regarding the Compton-Rayleigh peak ratio, the relationship between them is the expected for this type of matrices. Nonetheless, the tibia shows less intense peaks for most elements, and there is no detectable presence of Cu.

On average, trabecular bone (ribs) absorbs twice as much trace elements than compact bone (tibia), in *ante-mortem* conditions, although in *post-mortem* conditions, this values can be several orders of magnitude higher, due to the bone's exposure to elements present in the soils. Being the rib cage bones more vulnerable due to their porosity, their absorption of trace elements is greater [51]. This differences in the type of bone structure in each one of the samples could explain the differences in the elemental concentrations for bones of the same individual.

Figure 5.12 shows the overlapping of the spectra obtained with a portable XRF spectrometer with a planar 90º geometry (previously described in section 5.4) and a spectra

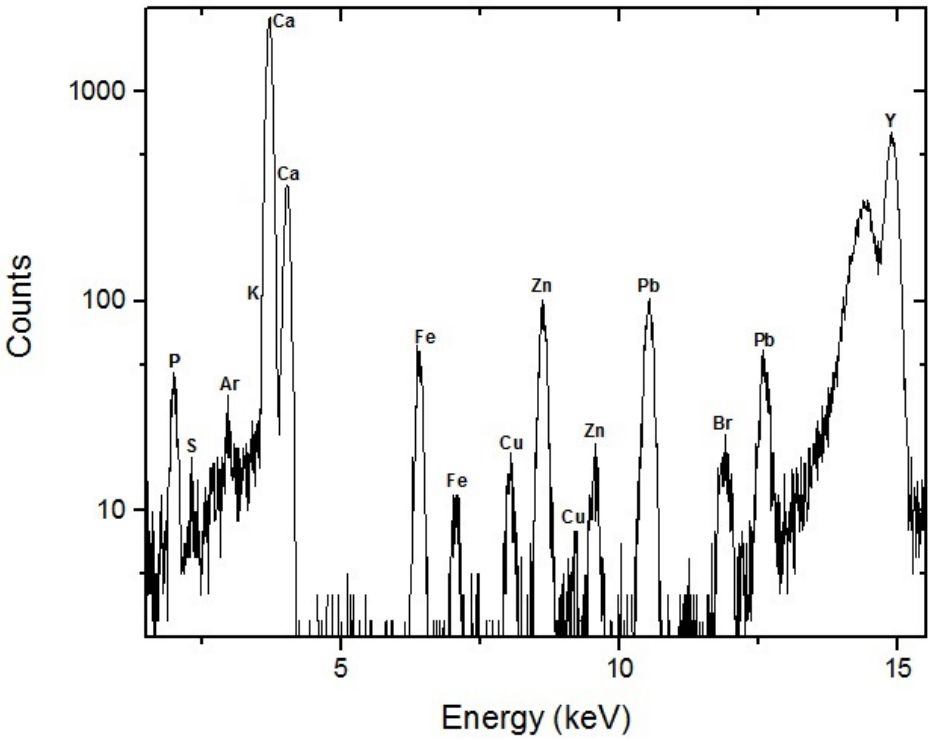

Figure 5.11: Rib pellet spectrum from Individual 54

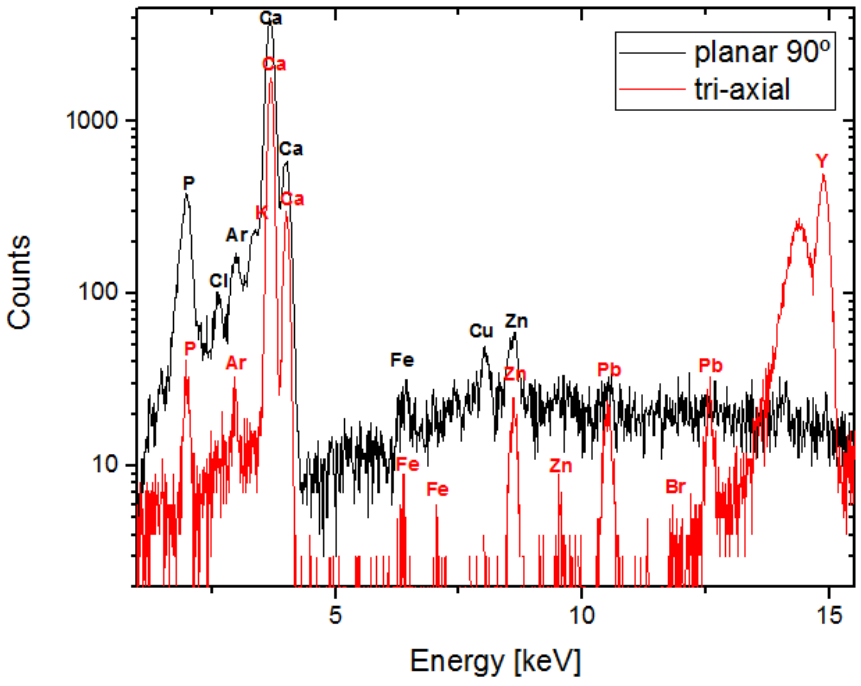

Figure 5.12: Overlapping of the spectrum of the tibia pellet from individual 54 acquired with the portable tri-axial set up, and with the portable planar 90º setup.

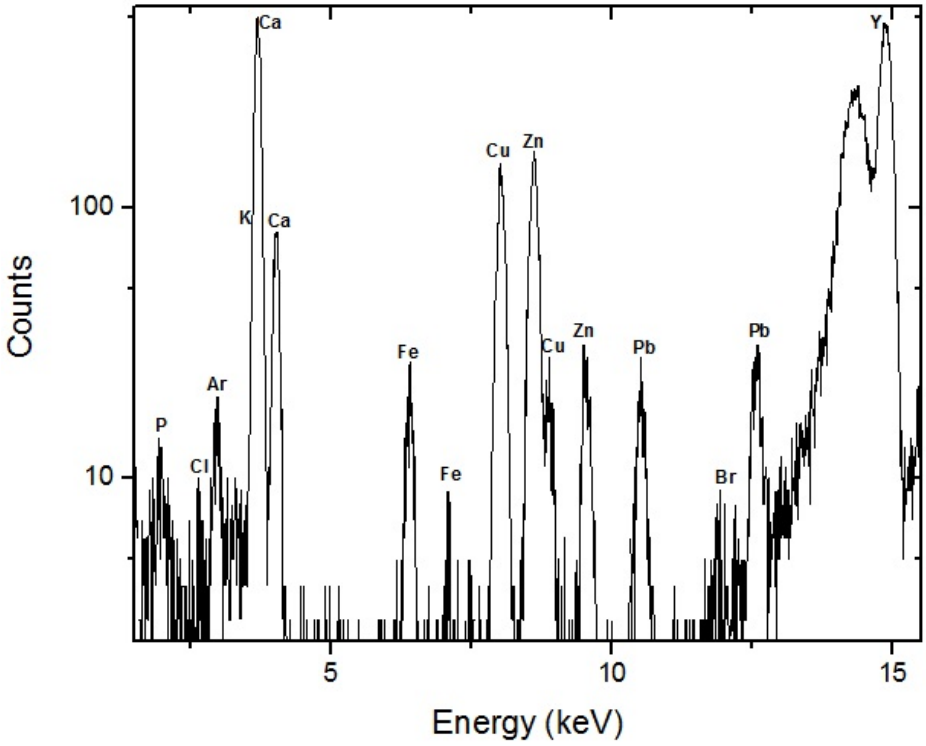

Figure 5.13: Femur bone spectrum from individual EES-E8A3C

obtained with the tri-axial setup, for the tibia pellet sample. Regarding the spectra obtained with the tri-axial geometry, the same observations apply as the ones made for the Rib pellet, although the peak-background ratio is lower. Comparatively with the planar setup, it is clear that the tri-axial geometry does indeed remove a great deal of the background, increasing the peak-background ratio.The tri-axial geometry is capable of identifying more elements in the range from 5 to 14 keV with very well defined peaks (Fe, Zn, Pb, Br) when compared with the planar spectrometer. The Cu peak present on the planar spectrometer's spectrum is due to a contamination of the spectrometer's setup, for other analysis of this sample showed no Cu. However, the planar geometry spectrometer can identify lighter Z elements, like chlorine, whose ionization cross-section is too low to be excited by the tri-axial setup and it's excited by the continuous radiation in the planar geometry's spectrometer. Overall the tri-axial setup has a better performance, regarding this type sample, but both spectrometers complement each other in identifying different elements.

As for the femur spectrum, in figure 5.13, even though the matrix of the sample is the same as the other bone samples, and bone reference standard materials, for this spectrum the whole bone was analyzed, alternatively to the bone powder pressed pellets. Due to different sample preparation and size of the samples, a quantitative comparison can not be made,but a qualitative one can be established. Shape wise, and elemental nature, the femur shows a spectrum similar to the Rib and Tibia spectrum, even tough the overall intensity was lower. Figure 5.14 shows a photograph of the setup during data acquisition

Figure 5.14: Tria-axial XRF set up and femur (EES-E8A3C)

of the femur bone.

With regard to the accuracy of our method, we compared the quantifications made with this dissertation's spectrometer versus a bench top triaxial geometry spectrometer with a molybdenum secondary target, and the detection was done with a Si(Li) detector, with a 30 mm^2 active area and a 8 μm beryllium window. The operation voltage was 50 kV and 20 mA, with 1000s acquisition time. The beam's spot size on sample was 1.5 cm and 2,0 cm [51].
From table 5.7 one can observe that the concentration values are in concordance and of the same order of magnitude with the valus obtained with the bench top spectrometer. However, these values are expected to differ, giving the fact that the bench top possesses a better sensitivity (as compared previously). Nonetheless, these are very satisfactory results.

Table 5.7: Concentration $mg.g^{-1}$ comparison for Tibia and Ribs from individual 54 with the portable tri-axial XRF system and a bench top tri-axial XRF system.

	Concentration for different bones [$\mu g.g^{-1}$]	
	Bench Top Tri-axial [50 kV 20 mA]	
	Tibia	Ribs
Ca	$37 \times 10^4 \pm 1 \times 10^4$	$39 \times 10^4 \pm 2 \times 10^4$
Zn	$1,1 \times 10^2 \pm 0,1 \times 10^2$	$5 \times 10^2 \pm 0,3 \times 10^1$
Pb	$1,2 \times 10^2 \pm 0,1 \times 10^2$	$5,6 \times 10^2 \pm 0,3 \times 10$
	Portable Tri-axial [40 kV 1 mA]	
	Tibia	Ribs
Ca	$28,8 \times 10^4 \pm 0,7 \times 10^4$	$36,2 \times 10^4 \pm 0,6 \times 10^4$
Zn	$1,4 \times 10^2 \pm 0,2 \times 10^2$	$5,9 \times 10^2 \pm 0,3 \times 10^2$
Pb	$8 \times 10^1 \pm 2 \times 10^1$	$2,8 \times 10^2 \pm 0,3 \times 10^2$

5.6.2 Analysis of a paper document signed by queen Maria the first of Portugal

Figure 5.15 corresponds to the overlapping of the spectra of the document acquired with this dissertation spectrometer, and the other acquired with a portable planar 90º XRF spectrometer (previously described in section 5.4, in table 5.3). One of the noticeable differences between both spectra, is the lower (almost non-existent) background radiation of the tri-axial spectrometer, when compared with the planar geometry one. When zooming in the spectra, from 1 keV to 10 keV, it is evident that the planar spectrometer allows for elemental detection in lower energy areas that the tri-axail does not, up until the 3 keV region, the planar allows to observe Si, S and Cl lines, not detected with the tri-axial. The rest of the elements in this first region are mostly detected with both spectrometers. The composition of this document was already analyzed in "X-ray fluorescence spectrometry on paper characterization: A case study on XVIII and XIX century documents", in which the presence of Co, Ni, As, Pb and Bi was detected [53]. The most prominent advantaged of the tri-axial lies on the detection of higher Z elements, (from 4 keV to 14 keV), allowing to identify elements such as Pb, and Bi, which are the elements that differentiate this type of paper.

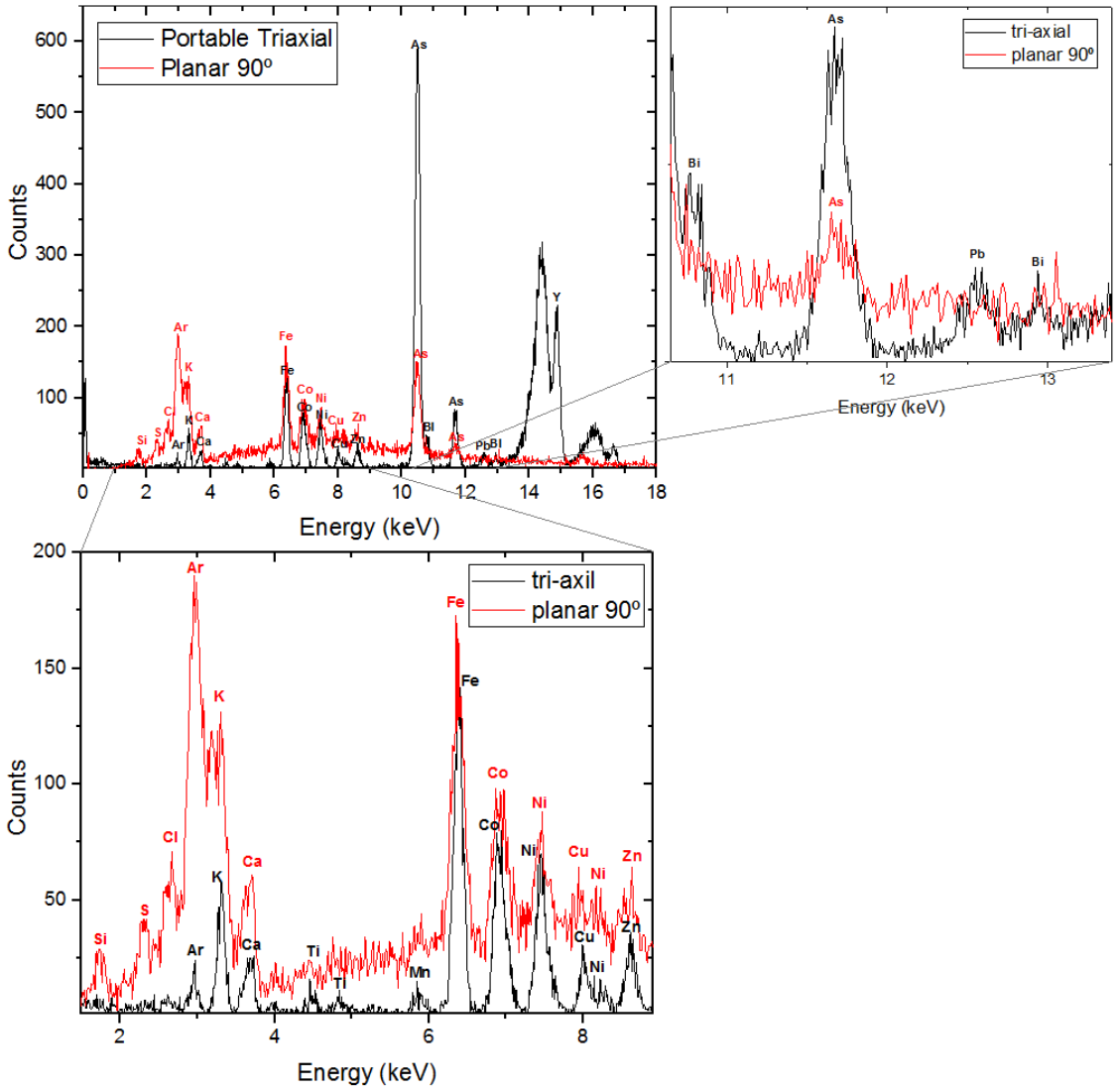

Figure 5.15: Overlapping of the spectra obtained with two different spectrometers of a document from 1779 signed by the queen of Portugal Maria the first

In section 4.1 the nature of this document was already described. Even though the document's paper matrix is quite similar to the reference standard samples with leaves matrices used in this dissertation, we will not use these samples to quantify the elements present in the sample. This is based on the grounds that the document's dimensions are not compatible with the ones of the leaves matrices, for the paper is much thinner than the pressed pellets. Nevertheless, a quantitative analogy can still be established between both samples. Figures 5.16 and 5.17 show the setup for the documents analysis in both spectrometers.

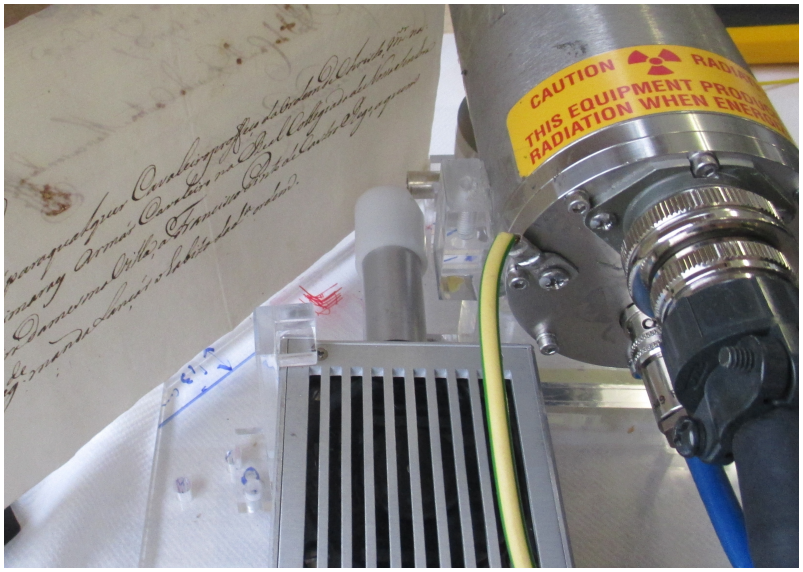

Figure 5.16: Tria-axial XRF set up and paper document

Figure 5.17: Planar 90º XRF set up and paper document

6 Conclusions and Outlook

The aim of this master thesis was to design and assemble a portable X-ray fluorescence spectrometer with a tri-axial geometry capable of performing analyses of samples with special interest in cultural heritage.

Firstly, the setup was designed, as described in chapter 3.2, the necessary material was manufactured, and the entirety was assembled and tested to ensure the proper operation of the spectrometer, as portrayed in section 3.3.

This technique is known for its various advantages: it is non-destructive, doesn't require sample preparation, allows for multi-elemental analyses. In particular, the tri-axial setup allowed both the monochromatization and polarization of the background radiation, leading to an improvement of the peak-to-background ratio. The use of a silver collimator between the secondary target and sample granted the correct direction of the beam, and the silver collimator at the detector's entrance helped reduce the incomplete charge collection, boosting this system's performance. The built spectrometer allowed the detection of elements with K and L line energies ranging from 2 keV to 14 keV, such as S, Ar, K, Ca, Ti, Cr, Mn, Fe, Co, Ni, Cu, Zn, As, Br, Pb and Bi.

Concerning the quality of the analytic method used in the data analysis with the developed spectrometer, the results are very pleasing, for they showed great accuracy.

When comparing the designed tri-axial spectrometer with a bench top equipment with the same geometry, we obtained lower detection limits, as it would be expected due to the more powerful tube of the bench top equipment. However, the detection limits for the portable spectrometer are still within the same order of magnitude, and we were able to identify more elements in a metal matrix with our equipment as well, hence, losing some sensitivity can pay-off in terms of gain in portability.

Regarding the comparison between the tri-axial portable setup and the planar 90º setup, we can conclude that for energies ranging from 3 keV to 14 keV, the tri-axial spectrometer is able to identify more elements over the planar one (particularly heavier metals like Pb, and Bi), and the peak-background ratio is noticeably improved in our setup. However, for lower Z elements, with energies up to 3keV, the planar spectrometer is able to identify more elements, and has slightly improved accuracy, due to the *Bremsstrahlung* that excites such energies (with the tri-axial setup the continuous radiation is practically

eliminated). Overall we obtained better results with the portable tri-axial geometry, of particular added-value when detecting higher Z elements, comparatively with other XRF spectrometers, proving that this setup, besides being viable, it's also advantageous.

Although the tube's low power did not allow for abundant counts in the spectra, the setup's portability allows for *in situ* analysis, proving to be a major advantage for research field in which samples need to be analyzed on the site, or can not leave its storage facilities (such as museums and libraries).

The overall cost of this project was 471,1 €(not including the materials and instruments already available at the lab). The cost of a similar commercial equipment is in the order of tens of thousands of euros, considering that the X-ray tube and detector have to be purchased separately and then assembled.Hand-held commercial XRF spectrometers' prices can range from 20000 to 40000 euros [57].

Like any scientific project, there is always room for improvement, but due to time and resources limitations, there was a need to impose some boundaries on the coverage of this dissertation project. However, we suggest the following future improvements for this setup, such as experimenting with other collimators combinations, and designing an adaptable sample's holder. It would also be interesting to perform more extensive dosimetry studies, and test other types of matrices to have a wider range of elemental detection limits. Testing this setup with other X-ray tubes with the same power but different anodes could also be an interesting project, for with a different anode other energy regions could be analyzed. Also, purchasing a new power supply for the X-ray tube it is not as much an improvement as it is a necessity to continue to use this setup.

Bibliography

[1] X. Hou, Y. He, and B. T. Jones. "Recent Advances in Portable X-Ray Fluorescence Spectrometry". In: Applied Spectroscopy Reviews 39.January 2015 (2004), pp. 1–25. ISSN: 0570-4928. DOI: 10.1081/ASR-120028867. URL: http://www.tandfonline.com/doi/abs/10.1081/ASR-120028867.

[2] G. Vittiglio, S. Bichlmeier, P. Klinger, J. Heckel, W. Fuzhong, L. Vincze, K. Janssens, P. Engström, A. Rindby, K. Dietrich, D. Jembrih-Simbürger, M. Schreiner, D. Denis, A. Lakdar, and A. Lamotte. "A compact μ-XRF spectrometer for (in situ) analyses of cultural heritage and forensic materials". In: Nuclear Instruments and Methods in Physics Research 213 (2004), pp. 693–698. ISSN: 0168583X. DOI: 10.1016/S0168-583X(03)01687-2.

[3] M. Guerra, S. Longelin, S. Pessanha, M. Manso, and M. L. Carvalho. "Development of a combined portable x-ray fluorescence and Raman spectrometer for in situ analysis". In: Review of Scientific Instruments 85.6 (2014). ISSN: 10897623. DOI: 10.1063/1.4883188.

[4] A. Argyraki, M. H. Ramsey, and P. J. Potts. "Evaluation of Portable X-ray Fluorescence Instrumentation for in situ Measurements of Lead on Contaminated Land". In: The Analyst 122.8 (1997), pp. 743–749. ISSN: 00032654. DOI: 10.1039/a700746i. URL: http://pubs.rsc.org/en/content/articlehtml/1997/an/a700746i.

[5] A. Longoni, C. Fiorini, P. Leutenegger, S. Sciuti, G. Fronterotta, L. Struder, and P. Lechner. "A portable XRF spectrometer for non-destructive analyses in archaeometry". In: Nuclear Instruments and Methods in Physics Research, Section A 409.1-3 (1998), pp. 407–409. ISSN: 01689002. DOI: 10.1016/S0168-9002(98)00113-2.

[6] M. West, A. T. Ellis, P. J. Potts, C. Streli, C. Vanhoof, D. Wegrzynek, and P. Wobrauschek. "Atomic spectrometry updata-X-ray fluorescence spectrometry". In: Journal of Analytical Atomic Spectrometry 26.10 (2011), pp. 1919–1963. ISSN: 0267-9477. DOI: 10.1039/c1ja90038b. URL: [PDF].

[7] O. Gonzalez-Fernandez, M. Hidalgo, E. Margui, M. L. Carvalho, and I. Queralt. "Heavy metals' content of automotive shredder residues (ASR): Evaluation of environmental risk". In: Environmental Pollution 153.2 (2008), pp. 476–482. ISSN: 02697491. DOI: 10.1016/j.envpol.2007.08.002.

[8] M. Guerra, M. Manso, S. Pessanha, S. Longelin, and M. L. Carvalho. "Theoretical and experimental study on the angular dependence of scattering processes in X-ray fluorescence systems". In: X-Ray Spectrometry 42.5 (Oct. 2013), pp. 402–407. ISSN: 00498246. DOI: 10.1002/xrs.2491. URL: http://doi.wiley.com/10.1002/xrs.2491.

[9] S. Pessanha, M. Manso, A. Guilherme, M. Costa, and M. L. Carvalho. "Investigation of historical documents for forensic purposes by x-ray fluorescence spectrometry". In: Surface and Interface Analysis 42.5 (2010), pp. 419–422. ISSN: 01422421. DOI: 10.1002/sia.3085.

[10] S. Pessanha, A. Guilherme, and M. L. Carvalho. "Comparison of matrix effects on portable and stationary XRF spectrometers for cultural heritage samples". In: Applied Physics A: Materials Science and Processing 97.2 (2009), pp. 497–505. ISSN: 09478396. DOI: 10.1007/s00339-009-5251-x.

[11] M Guerra, M Manso, S Longelin, S Pessanha, and M. L. Carvalho. "Performance of three different Si X-ray detectors for portable XRF spectrometers in cultural heritage applications". In: Journal of Instrumentation 7.10 (2012), pp. C10004–C10004. ISSN: 1748-0221. DOI: 10.1088/1748-0221/7/10/C10004. URL: http://iopscience.iop.org/article/10.1088/1748-0221/7/10/C10004.

[12] A. Guilherme, S. Pessanha, M. L. Carvalho, J. M. F. dos Santos, and J. Coroado. "Micro energy dispersive X-ray fluorescence analysis of polychrome lead-glazed Portuguese faiences". In: Spectrochimica Acta - Part B Atomic Spectroscopy 65.4 (2010), pp. 328–333. ISSN: 05848547. DOI: 10.1016/j.sab.2009.12.010.

[13] M. Manso and M. L. Carvalho. "Elemental identification of document paper by X-ray fluorescence spectrometry". In: J. Anal. At. Spectrom. 22.2 (2007), pp. 164–170. ISSN: 0267-9477. DOI: 10.1039/B608361G. URL: http://pubs.rsc.org/en/content/articlehtml/2007/ja/b608361g.

[14] R. Grieken and A. Markowicz. Handbook of X-ray spectrometry: methods and tech. 1992.

[15] R. Jenkins. X-Ray Fluorescence Spectrometry. Second Edi. John Wiley & Sons, Ltd. ISBN: 0-471-29942-1.

[16] AMPTEK. URL: http://amptek.com/ (visited on 04/28/2015).

[17] Britannica. Auger Effect. URL: http://www.britannica.com/science/Augereffect (visited on 01/08/2016).

[18] R. Tertian and F. Claisse. Principles of Quantitative X-Ray Fluorescence Analysis. London: Heyden & Son Ltd, 1982.

[19] R. Klockenkamper. Total-reflection x-ray fluorescence analysis. New York: Wiley, 1996.

[20] Anrophysics. Medical Imaging: X-Rays. URL: https://sites.google.com/site/anrosphysics/ib-physics/medical-physics-option/3-medical-imaging-x-rays (visited on 05/04/2015).

[21] R. Jenkins, R. Gould, and D. Gedcke. Quantitative X-ray spectrometry. New York, 1981.

[22] Hyperphysics. Compton Scattering. URL: http://hyperphysics.phy-astr.gsu.edu/hbase/quantum/compton.html (visited on 06/20/2015).

[23] R Cesareo. "X-ray physics: interaction with matter, production, detection." In: la Rivista del Nuovo Cimento della Società Italiana di Fisica 23 (2000).

[24] O. University. Rays and geometrical optics. URL: http://www.physics.brocku.ca/PPLATO/h-flap/phys6{_}2.html (visited on 03/13/2016).

[25] L. Salgueiro and J. G. Ferreira. Introdução à física atómica e nuclear. Lisboa: Tipografia Matemática, 1975.

[26] C. Barkla. "Polarization in secondary Rontgen radiation". In: Royal Society of London 19 (1905).

[27] A. H. Compton and C. F. Hagenow. "A measurement of the polarization of secondary x-rays". In: Journal of the Optical Society of America (1917-1983) 8 (1924), pp. 487–+.

[28] D. Guimarães. "Measurement of Lead Concentration in Biological Tissues by Atomic Spectroscopy Techniques". PhD thesis. Universidade Nova de Lisboa, 2011.

[29] Merriam-Webster. Collimator. URL: http://www.merriam-webster.com/dictionary/collimator (visited on 01/10/2016).

[30] B. I. Kitov. "Spectrum function of polarizer-scattered x-ray tube radiation". In: X-Ray Spectrometry 34.1 (2005), pp. 52–55. ISSN: 1097-4539. DOI: 10.1002/xrs.786. URL: http://dx.doi.org/10.1002/xrs.786.

[31] K. Matsui, A. Ogawa, J. Kikuma, M. Tsunashima, T. Ishikawa, and S. Matsuno. "Polarization for the background reduction in EDXRF - the technique that does indeed work". In: Denver X-ray conference on Applications of X-ray Analysis 16.1 (2009), pp. 1–7.

[32] Hitachi. Vortex. URL: http://www.hitachi-hightech.com/hhs-us/product{_}detail/?pn=ana-vortex-60ex (visited on 04/28/2015).

[33] KETEK. URL: http://www.ketek.net/ (visited on 04/28/2015).

[34] GlennF.Knoll. Radiation Detection and Measurement. Hoboken, N.J.: Wiley, 2000.

[35] B Beckhoff, B Kanngiesser, N Langhoff, R Wedell, and H Wolff. "Handbook of Practical X-Ray Fluorescence Analysis". In: 128 (2006), pp. 15548–15548. ISSN: 00027863. DOI: 10.1021/ja069803y. URL: http://www.springerlink.com/index/10.1007/978-3-540-36722-2.

[36] R. Jenkins, R. Manne, R. Robin, and C. Senemaud. "Nomenclature system for X-Ray Spectroscopy". In: Pure and Applied Chemistry 63.5 (1991), pp. 735–746. DOI: 10.1002/xrs.1300200308.

[37] A. Williams. "Handbook of analytical techniques, Volume 1". In: (2001), p. 1182. URL: http://books.google.com/books?id=k9tGSwAACAAJ{\&}pgis=1.

[38] A. Rindby. Software for energy-dispersive X-ray fluorescence. Vol. 18. 3. 1989, pp. 113–118. DOI: 10.1002/xrs.1300180308. URL: http://doi.wiley.com/10.1002/xrs.1300180308.

[39] G. V. B Wehling, P Vandenabeele, L Moens, R Klockenkamper, A von Bohlen and M. d. R. Hooydonk. "Investigation of Pigments in Medieval Manuscripts by Micro Raman Spectroscopy and Total Reflection X-Ray Fluorescence Spectrometry". In: Mikrochim Acta 130 (1999).

[40] P. J. Custódio, M. L. Carvalho, F Nunes, S Pedroso, and A Campos. "Direct analysis of human blood (mothers and newborns) by energy dispersive X-ray fluorescence." In: Journal of trace elements in medicine and biology organ of GMS 19.2-3 (2005), pp. 151–8. ISSN: 0946-672X. DOI: 10.1016/j.jtemb.2005.09.002. URL: http://www.ncbi.nlm.nih.gov/pubmed/16325530.

[41] O. Instruments. Orford Instruments - Jupiter 5000 X-ray tube. URL: http://www.oxford-instruments.com (visited on 2015).

[42] Matsusada. High voltage power supplies for X-ray Fluorescence and X-ray Diffraction. URL: www.matsusada.com.

[43] Vortex. Vortex-EX Silicon Multi-Cathode X-Ray Spectrometer.

[44] R. Redus. "Digital Pulse Processors, Theory of Operation". In: (2009). URL: http://www.amptek.com/pdf/dpp{_}theory.pdf.

[45] Canberra. Winaxil. URL: http://www.canberra.com/cbns/products/cbns-software.asp (visited on 01/28/2016).

[46] NIST. URL: http://www.nist.gov/.

[47] Wolfram. Cone Angle. URL: http://mathworld.wolfram.com/Cone.html (visited on 04/04/2015).

[48] J. E. Turner. Atoms, Radiation, and Radiation Protection: Third Edition. Wiley-VCH Verlag GmbH & Co. KGaA, 2007, pp. 1–585.

[49] FDA. Radiation-Emitting Products. URL: http://www.fda.gov/ (visited on 02/16/2016).

[50] DGS. Radiações Ionizantes. URL: https://www.dgs.pt/saude-ambiental/areas-de-intervencao/radiacoes/ionizantes/enquadramento.aspx (visited on 02/16/2016).

[51] A. A. Dias, M. Carvalho, M. L. Carvalho, and S. Pessanha. "Quantitative evaluation of ante-mortem lead in human remains of the 18th century by triaxial geometry and bench top micro X-ray fluorescence spectrometry". In: J. Anal. At. Spectrom. 30.12 (2015), pp. 2488–2495. ISSN: 0267-9477. DOI: 10.1039/C5JA00340G. URL: http://xlink.rsc.org/?DOI=C5JA00340G.

[52] J. Serrao. Pequeno Dicionário de História de Portugal. Lisboa: Iniciativas Editoriais, 1976.

[53] M. Manso, M. Costa, and M. Carvalho. "X-ray fluorescence spectrometry on paper characterization: A case study on XVIII and XIX century documents". In: Spectrochimica Acta Part B: Atomic Spectroscopy 63.11 (Nov. 2008), pp. 1320–1323. ISSN: 05848547. DOI: 10.1016/j.sab.2008.07.001. URL: http://www.sciencedirect.com/science/article/pii/S0584854708002139.

[54] N. Serman. Processing the radiograph. 2000. URL: http://www.columbia.edu/itc/hs/dental/sophs/material/processing.pdf (visited on 03/01/2016).

[55] E. Marieb and K. Hoehn. Human Anatomy & Physiology. 2006, p. 1159. DOI: 10.1007/BF00845519.

[56] J. C. Silva. Manual de elaboração de Relatórios e Tratamento de Resultados Experimentais. Universidade Nova de Lisboa, 2009.

[57] Portable XRF Analyser and Price List. URL: https://www.911metallurgist.com/blog/portable-xrf-analyzer-price.

A Appendix 1 - Technical Drawings

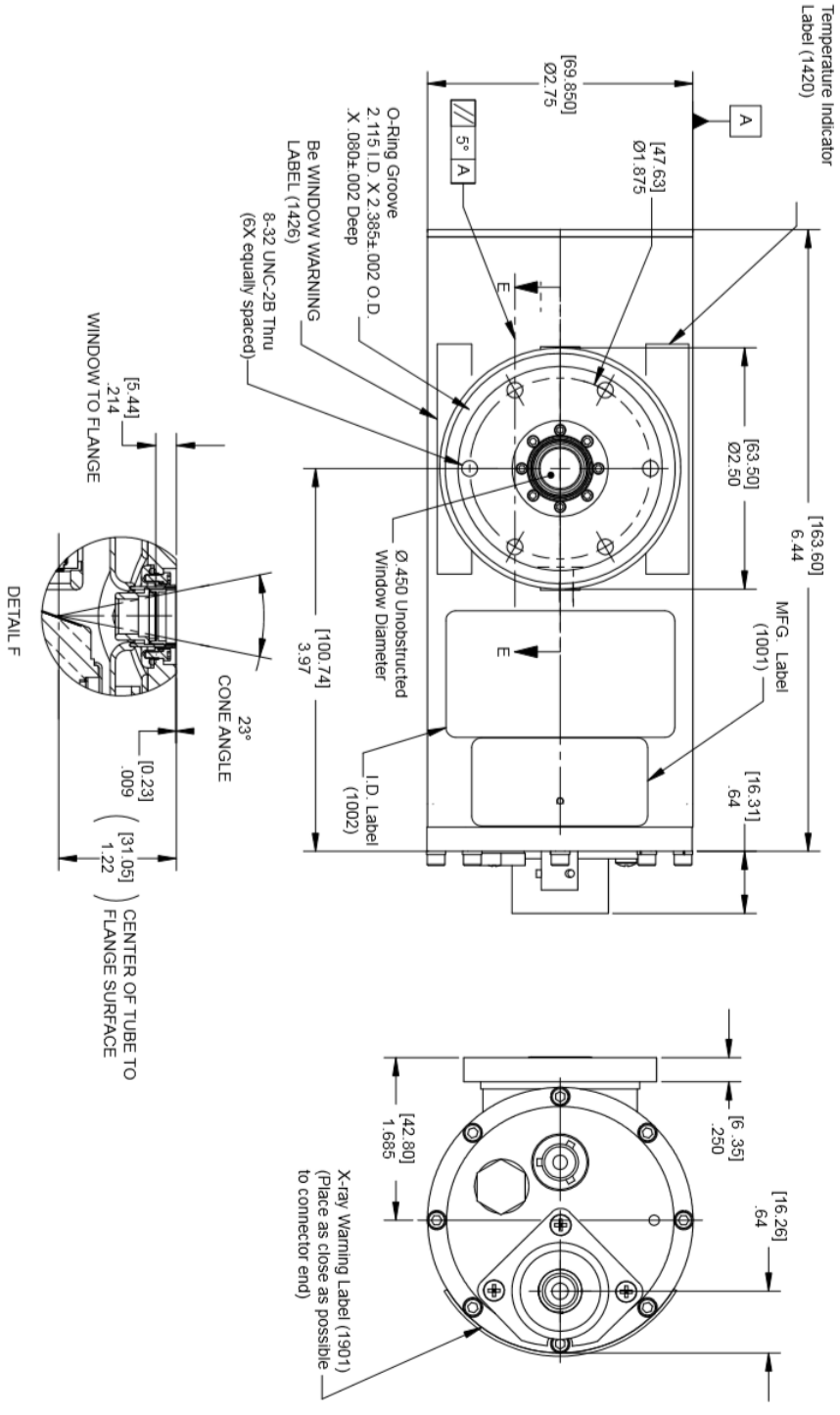

Figure A.1: X-ray tube - Technical Drawing [41]

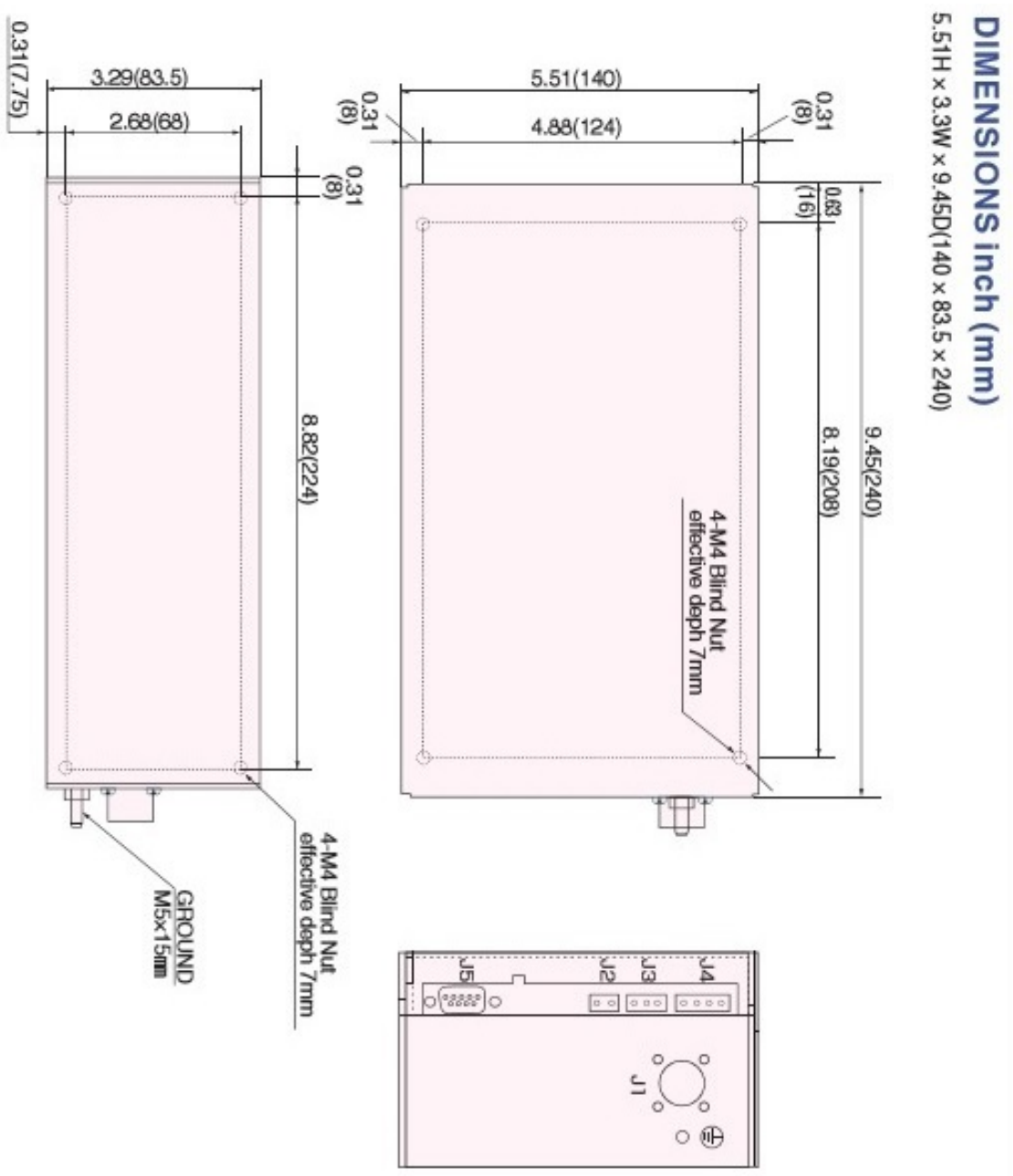

Figure A.2: X-ray power supply - Technical Drawing [42]

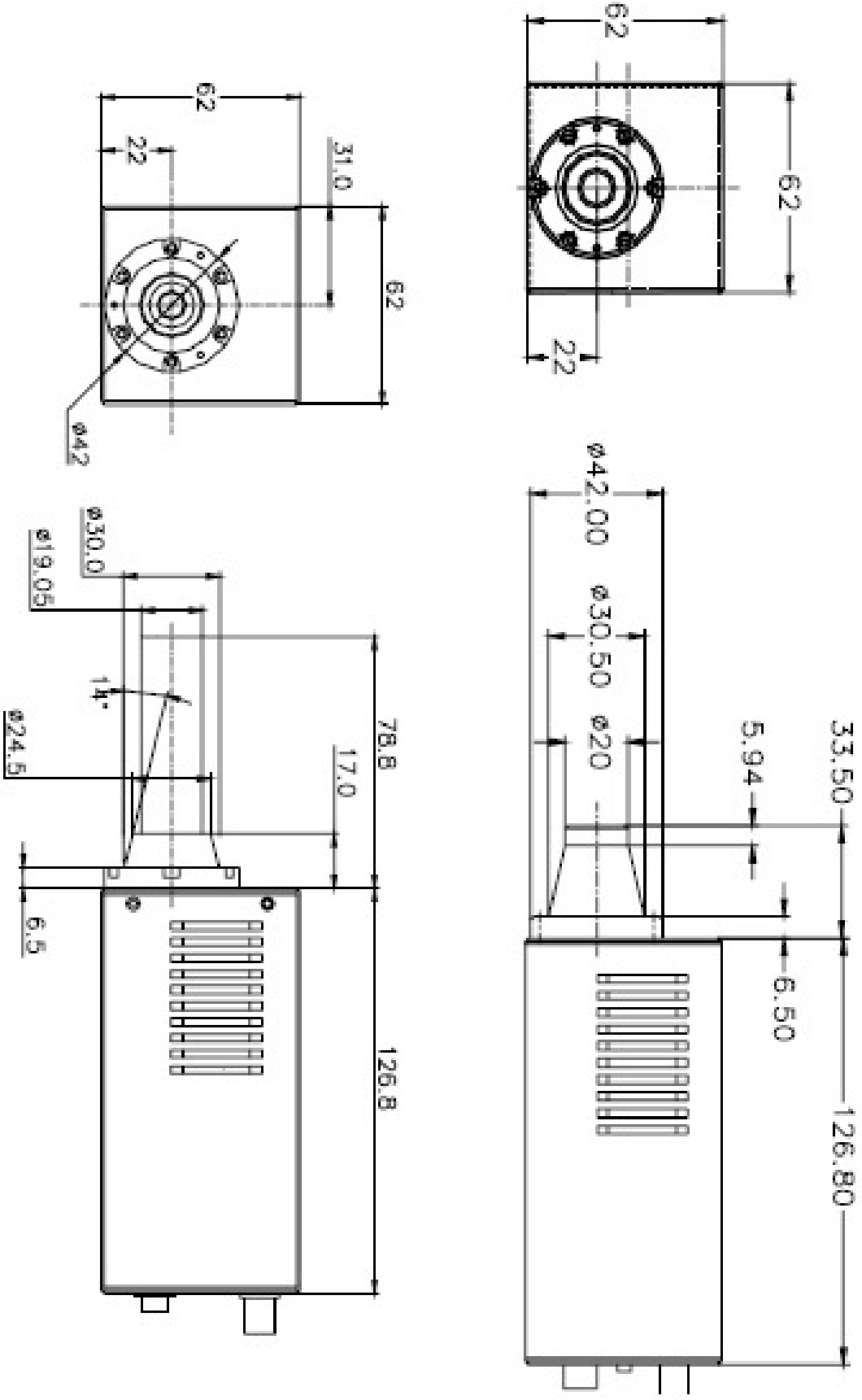

Figure A.3: Vortex detector - Technical Drawing [43]

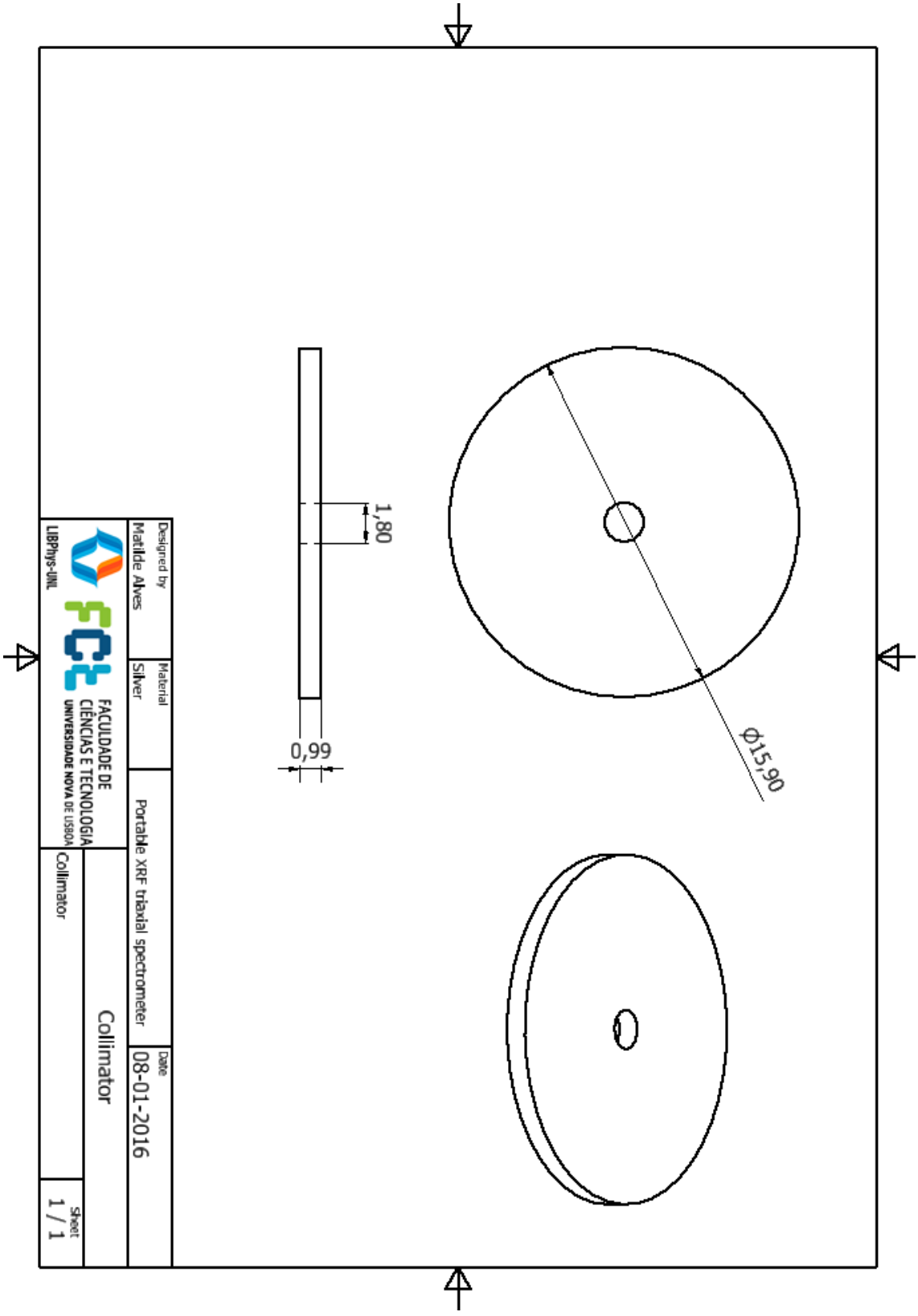

Figure A.4: Silver Collimator - Technical Drawing

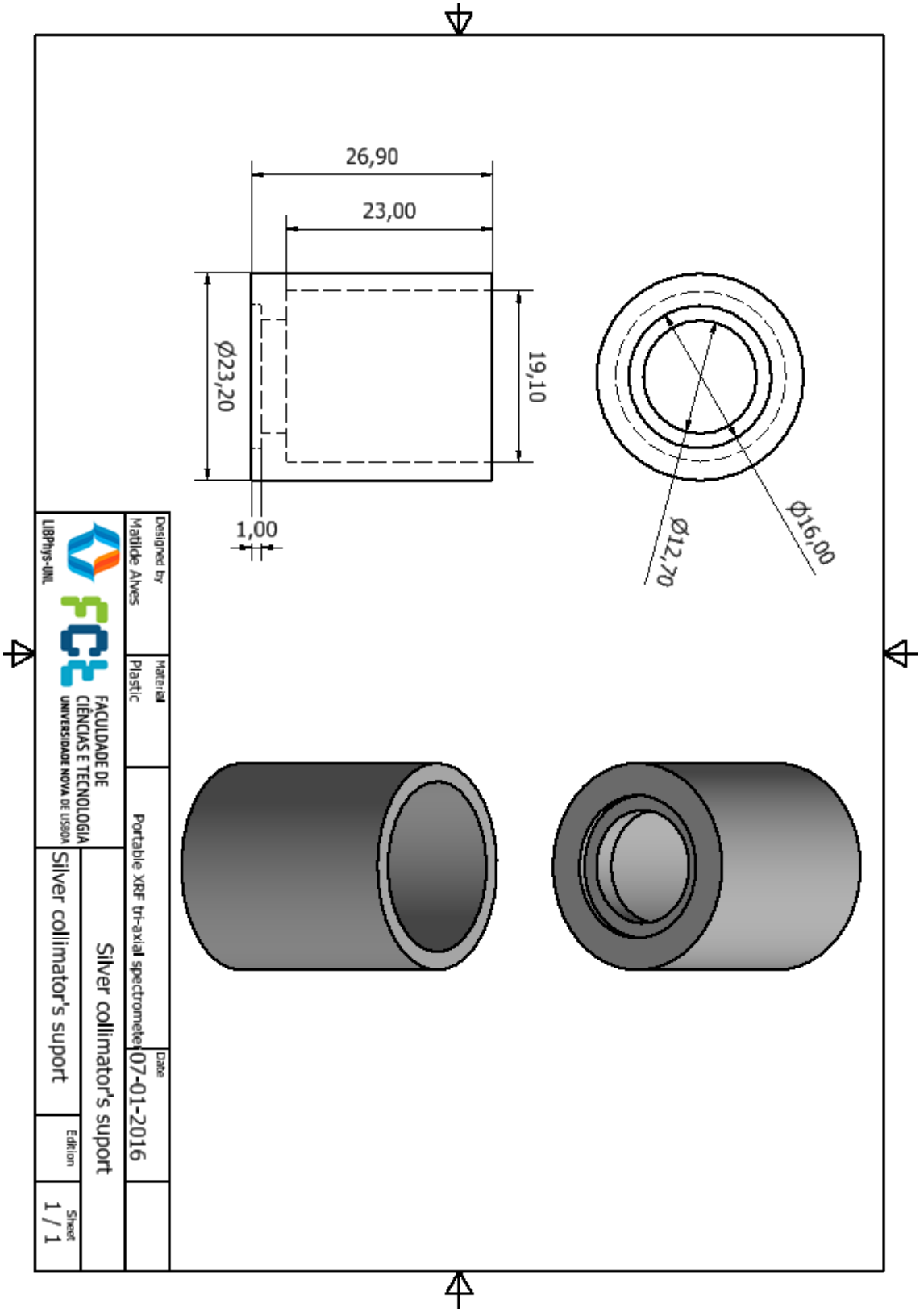

Figure A.5: Silver Collimator's support - Technical Drawing

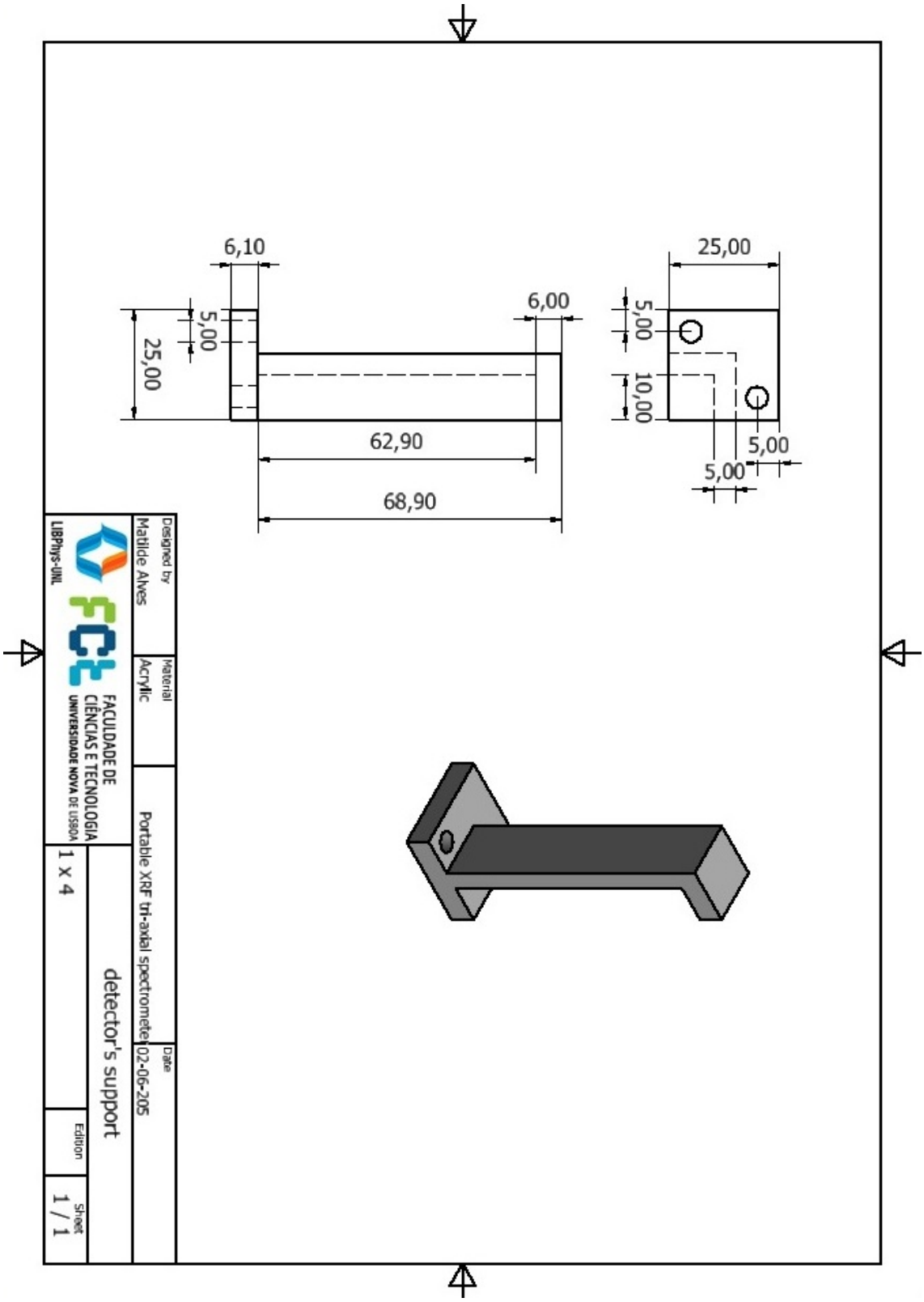

Figure A.6: Detector's support - Technical Drawing

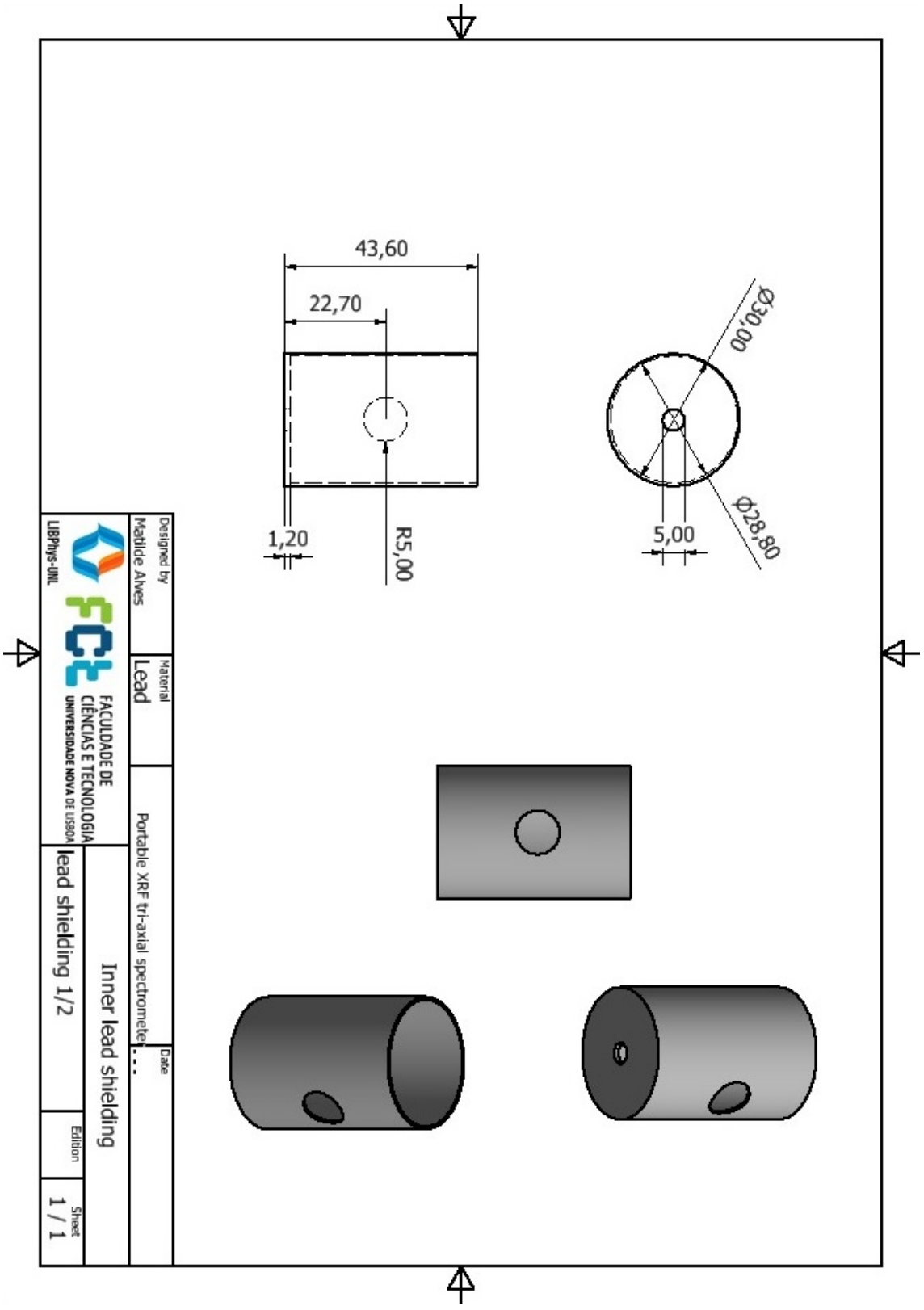

Figure A.7: Inner lead shielding- Technical Drawing

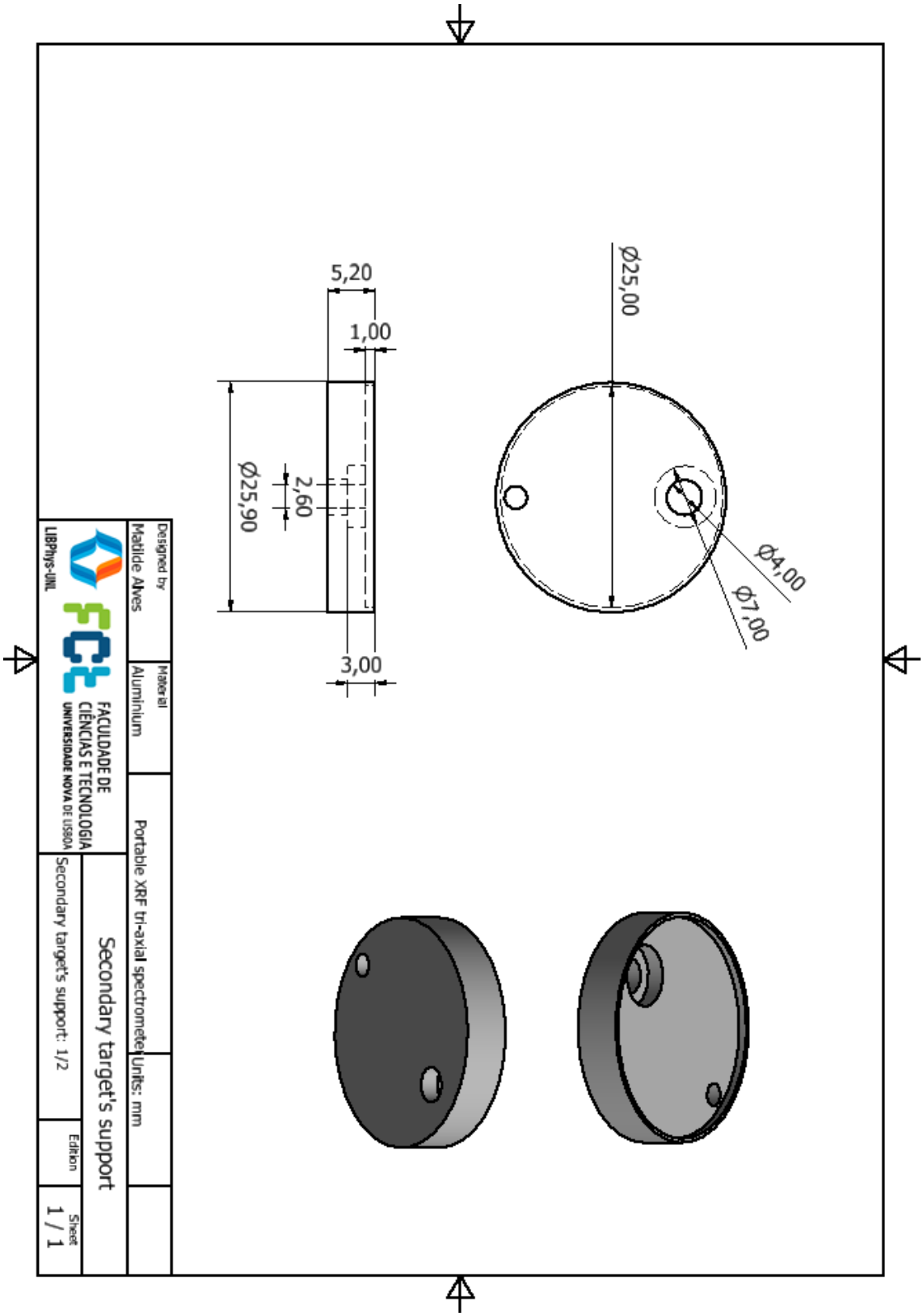

Figure A.8: Secondary target's support 1/2 - Technical Drawing

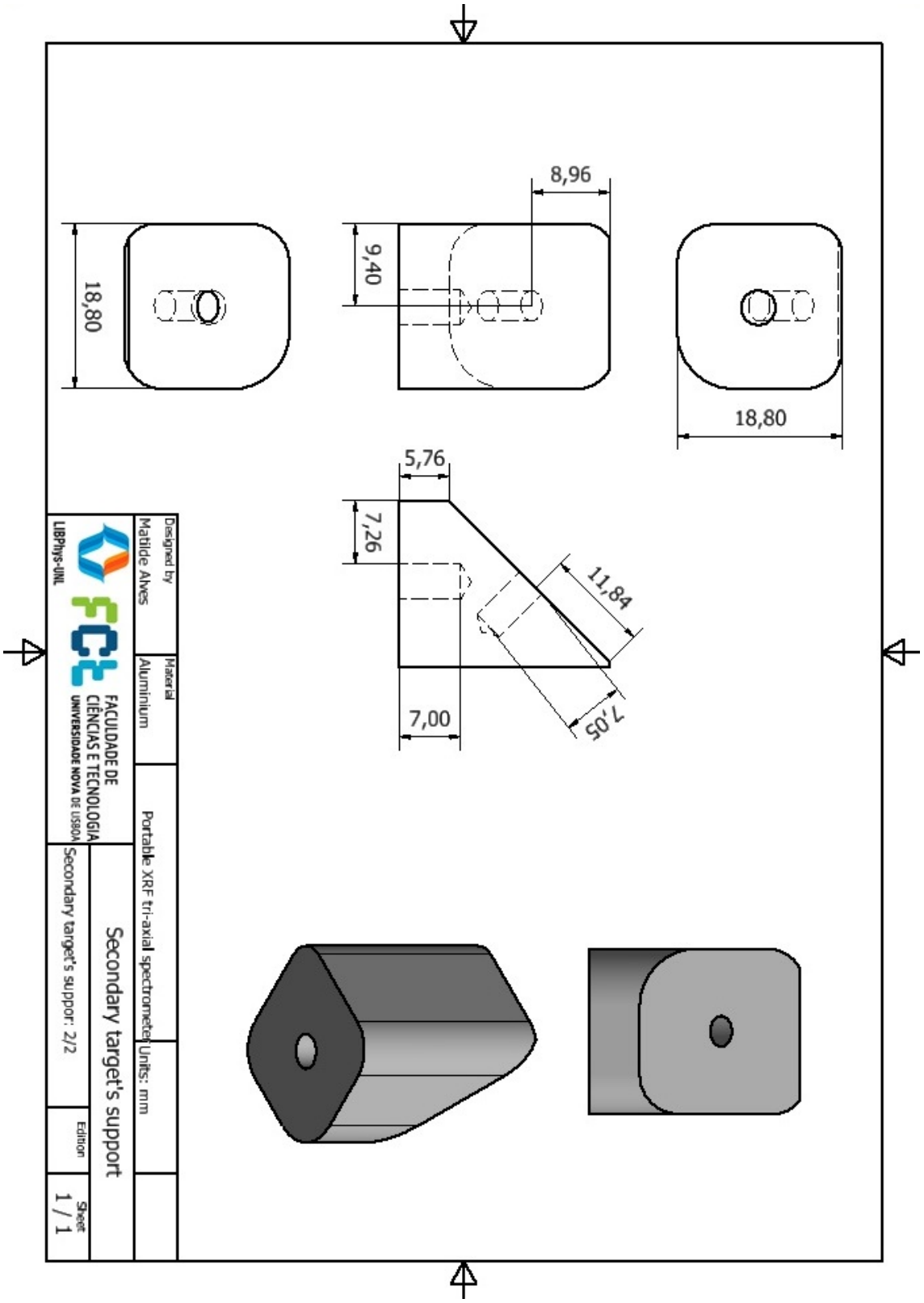

Figure A.9: Secondary target's support 2/2 - Technical Drawing

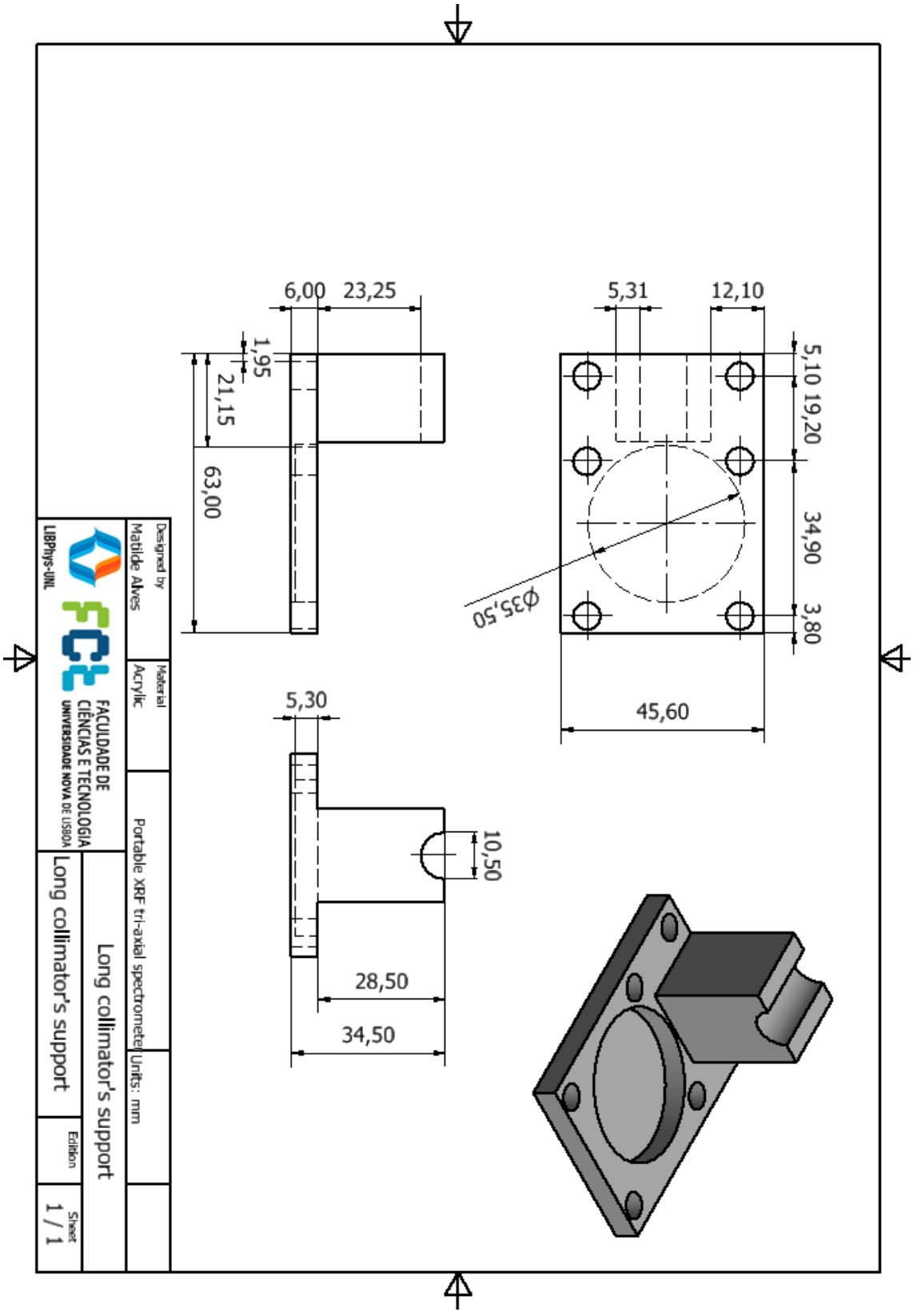

Figure A.10: Long collimator and secondary target's support - Technical Drawing

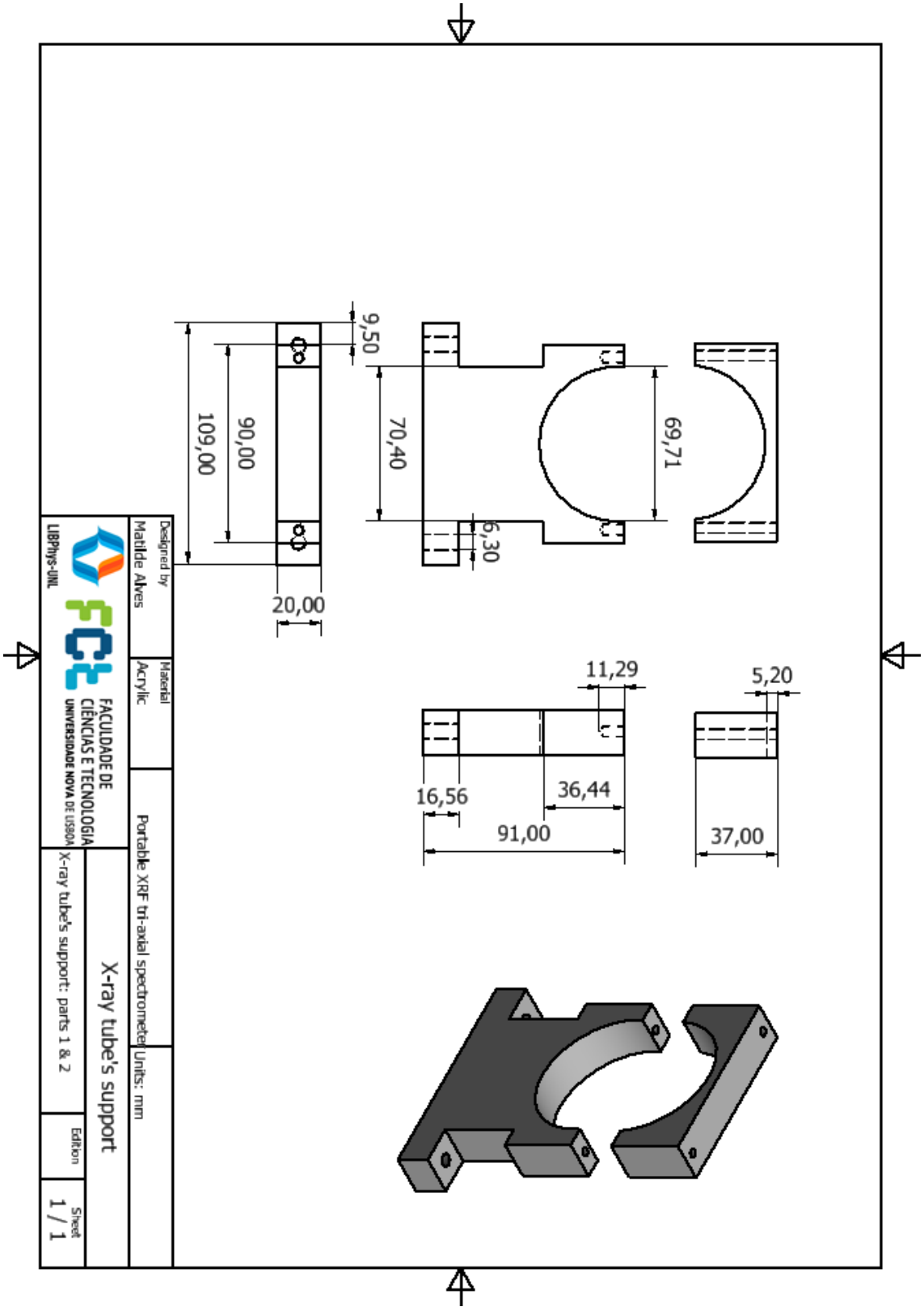

Figure A.11: X-ray tube's support - Technical Drawing

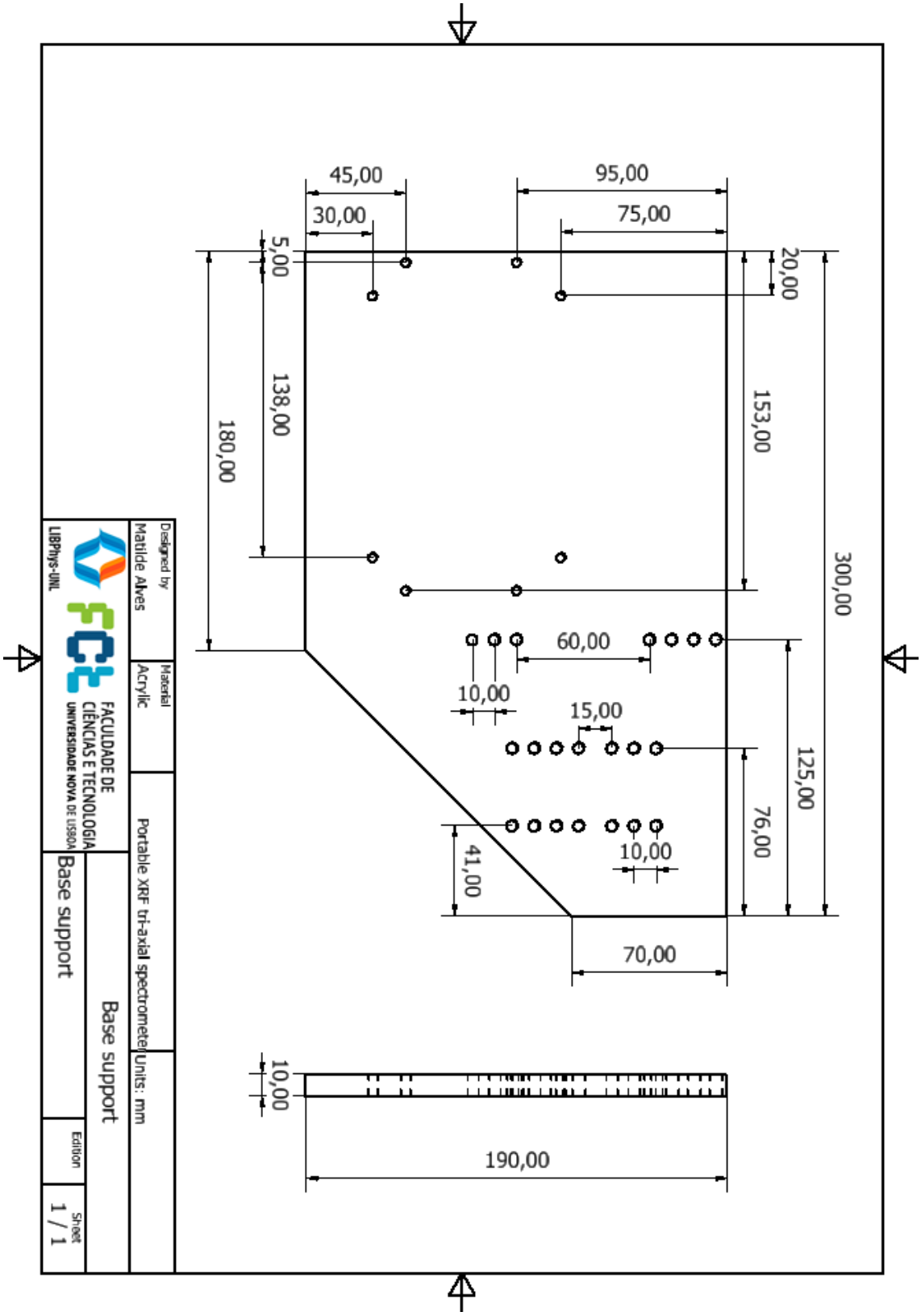

Figure A.12: Base support of the setup - Technical Drawing

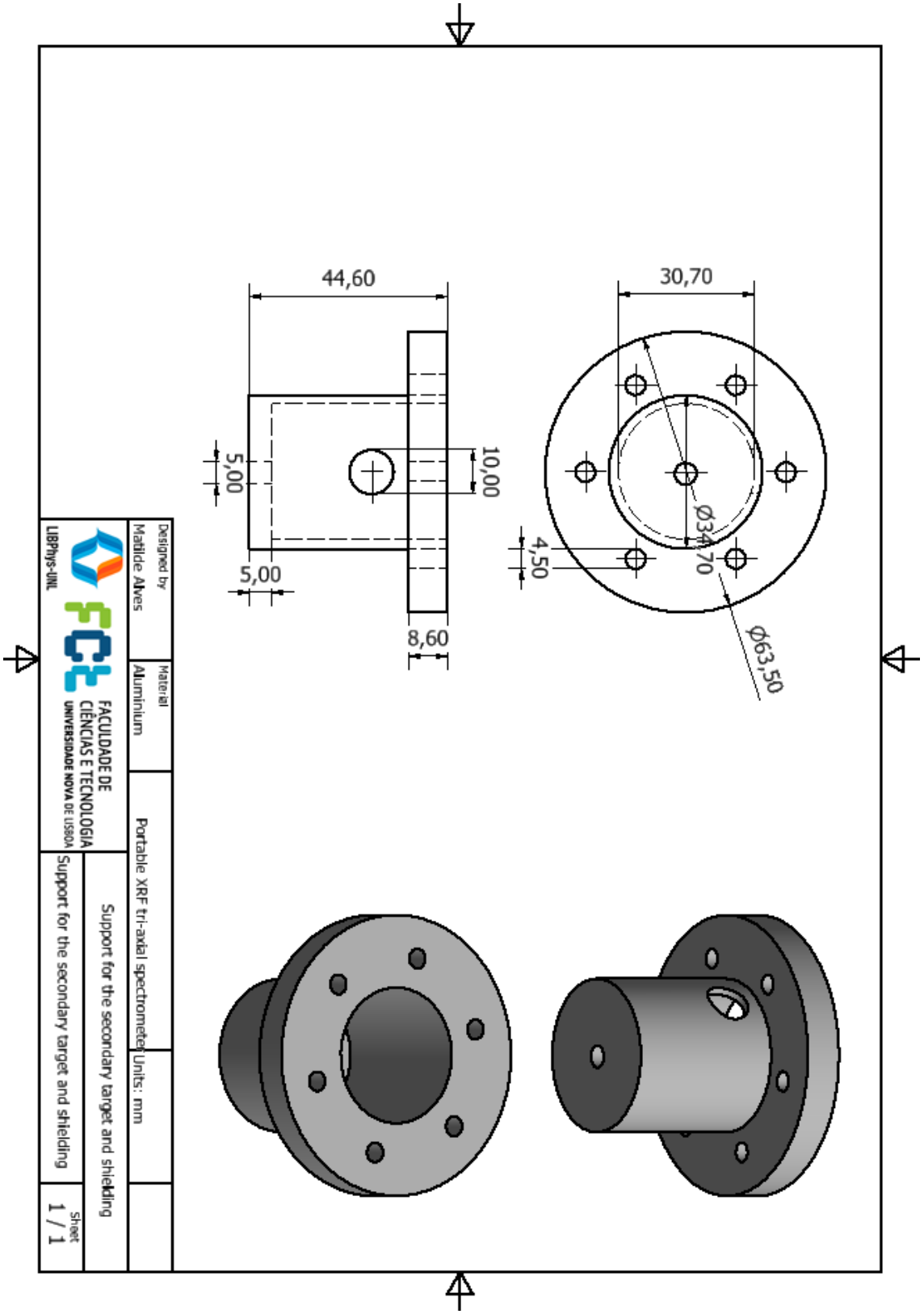

Figure A.13: Long collimator and secondary target's support - Technical Drawing